



## **X-Ray Amorphous Sulfur-Bearing Phases in Sedimentary Rocks of Gale Crater, Mars**

R. J. Smith, S. M. McLennan, B. Sutter, E. B. Rampe, E. Dehouck, K. L. Siebach, B. H. N. Horgan, V. Sun, A. Mcadam, N. Mangold, et al.

### **► To cite this version:**

R. J. Smith, S. M. McLennan, B. Sutter, E. B. Rampe, E. Dehouck, et al.. X-Ray Amorphous Sulfur-Bearing Phases in Sedimentary Rocks of Gale Crater, Mars. *Journal of Geophysical Research. Planets*, 2022, 127 (5), pp.e2021JE007128. 10.1029/2021JE007128 . insu-03682336

**HAL Id: insu-03682336**

**<https://insu.hal.science/insu-03682336>**

Submitted on 12 Oct 2022

**HAL** is a multi-disciplinary open access archive for the deposit and dissemination of scientific research documents, whether they are published or not. The documents may come from teaching and research institutions in France or abroad, or from public or private research centers.

L'archive ouverte pluridisciplinaire **HAL**, est destinée au dépôt et à la diffusion de documents scientifiques de niveau recherche, publiés ou non, émanant des établissements d'enseignement et de recherche français ou étrangers, des laboratoires publics ou privés.

# X-ray amorphous sulfur-bearing phases in sedimentary rocks of Gale crater, Mars

R. J. Smith<sup>1\*</sup>, S. M. McLennan<sup>1</sup>, B. Sutter<sup>2</sup>, E. B. Rampe<sup>3</sup>, E. Dehouck<sup>4</sup>, K. L. Siebach<sup>5</sup>, B. H. N. Horgan<sup>6</sup>, V. Sun<sup>7</sup>, A. McAdam<sup>8</sup>, N. Mangold<sup>9</sup>, D. Vaniman<sup>10</sup>, M. Salvatore<sup>11</sup>, M. T. Thorpe<sup>12</sup>, and C. N. Achilles<sup>8</sup>

<sup>1</sup>Department of Geosciences, SUNY Stony Brook, Stony Brook, NY 11794, USA

<sup>2</sup>Jacobs JETS at NASA Johnson Space Center, Houston, TX 77058, USA

<sup>3</sup>Astromaterials Research and Exploration Science Division, NASA Johnson Space Center, Houston, TX 77058, USA

<sup>4</sup>Univ Lyon, UCBL, ENSL, UJM, CNRS, LGL-TPE, F-69622, Villeurbanne, France

<sup>5</sup>Earth, Environmental and Planetary Sciences, Rice University, TX 77005, USA

<sup>6</sup>Department of Earth, Atmospheric, and Planetary Sciences, Purdue University, West Lafayette, IN 47907, USA

<sup>7</sup>Jet Propulsion Laboratory, California Institute of Technology, Pasadena, CA 91109, USA

<sup>8</sup>NASA Goddard Space Flight Center, Greenbelt, MD 20771, USA

<sup>9</sup>Laboratoire de Planétologie et Géodynamique, UMR6112, CNRS, Université de Nantes, France

<sup>10</sup>Planetary Science Institute

<sup>11</sup>Department of Astronomy and Planetary Science, Northern Arizona University, Flagstaff, AZ, 86011, USA

<sup>12</sup>Texas State University, JETS, at NASA Johnson Space Center, Houston, TX 77058, USA

\*Corresponding author: Rebecca Smith (rebecca.j.smith@stonybrook.edu)

## Key Points:

- A large percentage of the bulk SO<sub>3</sub> in Gale crater sedimentary rocks is in the X-ray amorphous state (20-90%).
- X-ray amorphous S-bearing phases are likely mixtures of Mg, Fe, Ca and other cation sulfates present as cement and in diagenetic features.
- In situ detections of X-ray amorphous SO<sub>3</sub> likely contribute to orbital spectral detections of sulfates in lower Mount Sharp.

## Abstract

The Curiosity rover in Gale crater is investigating the transition from the “clay -bearing unit” to the younger “sulfate-bearing” unit, which likely reflects a major aridification of the Martian climate. To fully understand this transition, we must characterize the sulfur-bearing phases encountered below it. The rocks below the transition have mostly crystalline Ca-sulfates with minor Fe-sulfates, and often have some fraction of their bulk SO<sub>3</sub> in the X-ray amorphous state with a poorly constrained nature. Here, we characterize the abundances and compositions of the X-ray amorphous sulfur-bearing phases in 19 drill samples using mass balance calculations, as well as evolved SO<sub>2</sub> gas measured by the SAM instrument for a subset of 5 samples. We find that ~20-90 wt% of a sample’s bulk SO<sub>3</sub> is in the X-ray amorphous state and that X-ray amorphous sulfur-bearing phase compositions are consistent with mixtures of Mg-S, Fe-S, and

possibly Ca-S phases, likely sulfates or sulfites. These materials reside in the bedrock, perhaps as cementing agents deposited either with the detrital sediments or during early diagenesis, and in diagenetic alteration halos likely deposited after lithification during late diagenesis. Many rocks have large fractions of X-ray amorphous Mg-S phases, possibly highly soluble Mg-sulfates, suggesting negligible fluid flow through the bedrock post-Mg-sulfate deposition. X-ray amorphous sulfur-bearing materials likely contribute to orbital spectral detections of sulfates, and so our results help form multiple hypotheses to be tested in the sulfate unit and are important for understanding the evolution of the Martian surface environment at Gale crater.

## **Plain Language Summary: (should be 200 words)**

The Curiosity rover in Gale crater, Mars is investigating a mineral transition observed from orbit – older clay-rich to younger sulfur-rich rocks - that likely reflects a change from a wetter to a drier Martian climate. Many of the sedimentary rocks investigated by the rover below the mineral transition have X-ray amorphous sulfur-bearing phases that are poorly constrained. To fully appreciate the significance of the transition to more sulfate-rich rocks, we must understand the abundance and compositions of the X-ray amorphous sulfur-bearing phases present below the transition. Here, we investigate the X-ray amorphous sulfur-bearing phases at 19 drill sites below the transition. We find that most rocks have large fractions of X-ray amorphous sulfur-bearing phases that are likely mixtures of Mg-, Fe-, and possibly Ca-sulfates or sulfites. In some rocks, X-ray amorphous sulfur-bearing phases might have precipitated from solutions delivered to the lake early on and could be cementing sediment grains. In other locations, X-ray amorphous sulfur-bearing phases are associated with zones where fluids altered the rocks long after they were cemented. These results help form multiple hypotheses to be tested in the sulfate-rich rock unit and are important for understanding the evolution of the Martian surface environment at Gale crater.

## **1 Introduction:**

One reason why the Mars Science Laboratory (MSL) mission was sent to Gale crater, Mars was because orbital observations indicated that the central mound, Aeolis Mons, comprises relatively flat-lying layered rocks that transition from stratigraphically lower (older) rock units with clay/sulfate mineral spectral signatures to stratigraphically higher (younger) rock units with sulfate/oxide spectral signatures (Milliken et al., 2010). This spectrally significant clay-sulfate mineral transition has been noted in other locations on Mars (e.g., Bibring et al., 2006; Carter et al., 2013) and is thought to preserve a period of global scale climate change in Mars' history from a wetter to a more arid climate, possibly leading ultimately to the inhospitable conditions found on the surface today (Bibring et al., 2006). To fully appreciate the nature, extent and implications of this transition, it is important to “ground truth” the observation by investigating the textures and chemistry of the sulfur-bearing mineral phases along the rover traverse and into the mineralogical transition.

A range of sulfur-bearing mineral compositions has been observed in the sedimentary rocks examined by the *Curiosity* rover. To date, the Chemistry & Mineralogy (CheMin) X-ray diffractometer (XRD) (Blake et al., 2012) has detected mostly Ca-sulfates (gypsum, bassanite, and anhydrite) with Fe-sulfates (jarosite) detected in relatively low abundances in some locations (Vaniman et al., 2018; Rampe et al., 2020a). Notably, sulfides have not been identified above the CheMin detection limit ( $> \sim 1$  wt%) in any sample. The Sample Analysis at Mars (SAM)

instrument (Mahaffy et al., 2012) cannot detect Ca-sulfates, but SAM evolved gas analyses (EGA) for most drill sites indicate SO<sub>2</sub> release temperatures and peak shapes consistent with Fe- and Mg-sulfur-bearing materials. Additionally, EGA SO<sub>2</sub> traces and isotopic compositions show that most samples have oxidized S-bearing phases such as sulfates and sulfites with reduced sedimentary sulfides being important SO<sub>2</sub> contributors at only two locations (Franz et al., 2017). These observations indicate mostly oxidizing conditions during the deposition of the sulfur-bearing phases and the lack of detection of Mg-sulfates or sulfites (and in some cases Fe-sulfates) by CheMin indicates that these phases are either mixtures of crystalline phases present below CheMin detection limits and/or X-ray amorphous in nature.

X-ray amorphous phases are materials that either completely lack crystal structure (amorphous) or do not have sufficient consecutive planes of atoms to create detectable peaks in the X-ray diffraction patterns (Klug and Alexander, 1974). X-ray amorphous sulfur-bearing materials are not common geologic materials on Earth. Hypotheses for these phases on Mars include amorphous, nano-, or poorly crystalline sulfates formed through dehydration under current Martian surface conditions or as precursors to crystalline sulfates (e.g., Vaniman et al., 2004; Vaniman and Chipera, 2006; Wang et al., 2009; Sklute et al., 2015, 2018; Wang, Y. et al., 2012), sulfate anions adsorbed onto X-ray amorphous weathering products (e.g., allophane, ferrihydrite) (e.g. Rampe et al., 2016), and S-bearing phase inclusions in glass (McAdam et al., 2014; Sutter et al., 2017). Sulfur-bearing phase properties (e.g., abundance, crystallinity, composition) can be linked to environmental conditions such as relative humidity (RH), pH, oxidation state, and salinity, and so constraining these properties can help inform on the environments and processes that formed them.

Here, we use bulk X-ray amorphous component compositions calculated by Smith et al. (2021) and detailed SAM evolved SO<sub>2</sub> gas analyses to compare the abundances and compositions of the X-ray amorphous sulfur-bearing phases in most of the Gale crater rocks examined by CheMin below the mineral transition detected from orbit. These results are then used to speculate on the timing of deposition and their formation conditions. One of our findings, that between 20 and 90 wt% of a sample's bulk SO<sub>3</sub> is in the X-ray amorphous state, highlights the importance of this study as this observation indicates that large fractions of the sulfur-bearing phases present below the spectrally significant mineral transition have not been characterized. We discuss how these phases can allow us to better appreciate the geologic significance of the mineral transition and increase our understanding the history of water in Gale crater in general.

## 2 Background

### 2.1 Geologic Context

As of sol 2300 (January 24, 2019; a sol is a Martian day, numbered from the first sol of any mission), the *Curiosity* rover has worked its way up the slopes of Aeolis Mons, investigating ~380 vertical meters of the sedimentary rocks that make up the basal part of this ~5 km high topographic feature (e.g., Grotzinger et al., 2014, 2015). The Gale crater impact event has been dated to between ~3.6 and 3.8 Gy ago during the late Noachian/early Hesperian epochs (Thomson et al., 2011), and it is possible that the entire crater was filled with fluvial, lacustrine,

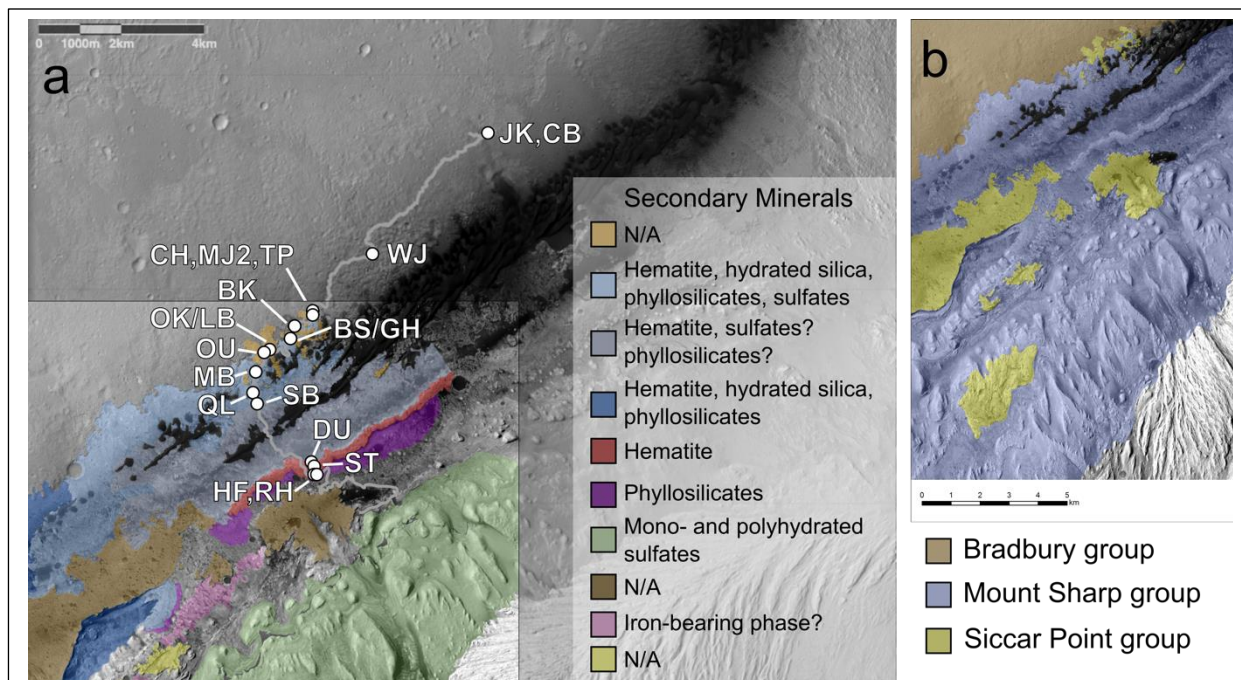


**Figure 1.** Modified from Fraeman et al. (2016). (a) Rover traverse (grey line) and drill hole locations (white dots) shown in context with major spectral units and interpreted secondary mineralogy as defined by Fraeman et al. (2016). (b) Figure from Fraeman et al. (2016) showing stratigraphic groups discussed in this study. Drill holes: JK—John Klein, CB—Cumberland, WJ—Windjana, CH—Confidence Hills, MJ—Mojave, TP—Telegraph Peak, BK—Buckskin, OU—Oudam, MB—Marimba, QL—Quela, SB—Sebina, DU—Duluth, ST—Stoer, HF—Highfield, RH—Rockhall, BS—Big Sky, OK—Okoruso, GH—Greenhorn, LB—Lubango.

and eolian sediments by the early Hesperian before being eroded through eolian processes (Malin and Edgett, 2000; Le Deit et al., 2013; Grant et al., 2014; Grotzinger et al., 2015). From orbit, the crater floor and lower strata of Aeolis Mons have spectral signatures consistent with alteration assemblages including hematite and phyllosilicates with variable hydrated sulfate and hydrated silica (Figure 1a; Fraeman et al., 2016). Higher up Aeolis Mons are strata with spectral signatures consistent with alteration assemblages dominated by monohydrated and polyhydrated sulfate minerals (a structure referred to as the “sulfate unit”). As of sol 2300, the most recent sampling date examined in this study, MSL had driven over 20 km laterally and gained 380 m of elevation but had not yet reached the mineral transition (Figure 1a). The three major stratigraphic units observed along the traverse and covered in this study are the Bradbury, Mount Sharp, and Siccar Point groups (Figure 1b).

The Bradbury group rocks make up part of the crater floor deposits (Grotzinger et al., 2015), and three Bradbury group drill samples were examined by CheMin: two lacustrine mudstones in the Yellowknife Bay formation, John Klein (JK) and Cumberland (CB) (see Figure 1a for sampling locations and name abbreviations used throughout the text), and one fine-grained sandstone consisting of reworked deltaic and eolian sediments located in the Kimberley formation, Windjana (WJ) (Rice et al., 2017; Vaniman et al., 2014; Treiman et al., 2016; Morrison et al., 2018). Both mudstone samples were found to have crystalline Ca-sulfates (anhydrite and bassanite) and were initially modeled with 1 wt% pyrrhotite, though subsequent analyses were not able to model pyrrhotite with confidence for either sample (e.g., Morrison et

al., 2018; Rampe et al., 2020a). Models of XRD data showed that the sandstone sample contained crystalline Ca-sulfates (anhydrite and bassanite), and the X-ray amorphous component was notably high in SO<sub>3</sub> and Cl (Treiman et al., 2016; Dehouck et al., 2017). Ca-sulfates are either completely or mostly associated with diagenetic features (e.g. veins, nodules, etc.; Vaniman et al., 2014; Nachon et al., 2014, 2017).

As of sol 2300, CheMin had analyzed 12 drill hole locations within the Mount Sharp group, which consists of mostly fluviolacustrine mudstones and fine-grained sandstones (e.g., Rivera-Hernández et al., 2020; Morris et al., 2016; Rampe et al., 2017, 2020b; Achilles et al., 2020). Most of these rocks have geochemical compositions distinct from sediments in the Bradbury group (Berger et al., 2020; Thompson et al., 2020), indicating a change in dominant sediment sources (Bedford et al., 2019) and degree of chemical alteration (e.g., Mangold et al., 2019; Hurowitz et al., 2017; Thorpe et al., 2021). The Mount Sharp group includes three targets on Vera Rubin ridge (VRR; between ~ -4190 and -4140 m), a topographic ridge that shows strong spectral signatures of hematite from orbit and from the ground, and is interpreted to have experienced substantial diagenetic alteration relative to the surrounding units (e.g., Fraeman et al., 2020; David et al., 2020; Horgan et al., 2020; L'Haridon et al., 2020; Rampe et al., 2020b). The first three drill samples in the Mount Sharp group, Confidence Hills (CH), Mojave2 (MJ2), and Telegraph Peak (TP) notably lacked crystalline Ca-sulfates, though Mojave2 did contain lenticular features interpreted as pseudomorphs after gypsum (Kah et al., 2018), and instead were found to contain jarosite (~1 wt% in CH, ~3 wt% in MJ2, and ~2 wt% in TP) (Rampe et al., 2017). Ca-sulfates reappeared in the Buckskin sample (~1 wt% anhydrite) but jarosite was absent (Rampe et al., 2017). Anhydrite was observed in all subsequent Mount Sharp group rocks through VRR with some locations also bearing gypsum and/or bassanite, as well as jarosite (Marimba, Quela, Sebina, Stoer, and Rock Hall) (Achilles et al., 2020; Rampe et al., 2020b).

The youngest strata considered in this study are the lithified eolian dunes comprising the Siccac Point group, which unconformably lie on top of some sections of the Mount Sharp group (Watkins et al., 2016; Banham et al., 2018). CheMin analyzed four drill samples within the Siccac Point group prior to sol 2300: two within parent bedrock, Big Sky (BS) and Okoruso (OK); and two within light-toned alteration “halos” surrounding central fractures, Greenhorn (GH) and Lubango (LB) (Yen et al., 2017). The fracture-associated alteration halos are silica-enriched zones ~50 cm wide that crosscut both the Mount Sharp and overlying Siccac Point group rocks (Frydenvang et al., 2017; Yen et al., 2017). These alteration halos have been interpreted as late diagenetic features that represent either chemical precipitates (Frydenvang et al., 2017) or leaching residue (Yen et al., 2017) and may have formed through multiple fluid episodes (Yen et al., 2017; Hausrath et al., 2018). The parent rocks were found to contain minor crystalline Ca-sulfates (anhydrite and bassanite) and the alteration halos had significant crystalline Ca-sulfates (anhydrite, bassanite, and gypsum) (Yen et al., 2017).

Multiple diagenetic events are recorded in the sedimentary rocks in Gale crater, but the timeframes for these processes are somewhat poorly constrained. Buried sediments underwent the diagenetic process of lithification, which includes porosity reduction through compaction and cementation (Worden and Burley, 2003). The cementing agents for Gale crater rocks are not well understood but likely consist of variable mixtures of syn-depositional to early diagenetic crystalline Fe oxides (magnetite and hematite; Blaney et al., 2014; Bristow et al., 2015; Hausrath et al., 2018; Tosca et al., 2018) and phyllosilicates (Bristow et al., 2015, 2018; Bridges et al., 2015), X-ray amorphous Fe oxides and silicates (Smith et al., 2021), and Ca-sulfate (e.g., Blaney

et al., 2014; Newsom et al., 2016; Rapin et al., 2019), with potential Mg-sulfate cemented layers in one ~10 m interval (Rapin et al., 2019).

The sedimentary rocks also contain evidence for diverse diagenetic processes spanning a range of timeframes. Early diagenetic features include lenticular crystal pseudomorphs after gypsum (likely deposited syndepositionally) in the Pahrump Hills section of the Mount Sharp group (Kah et al., 2018) and desiccation cracks in the Sutton Island member of the Mount Sharp group (Stein et al., 2018). Sections of the Sheepbed mudstone in the Bradbury group display syneresis cracks filled with cement (fracture-filling raised ridges) likely comprised of Mg-rich, Al-deficient smectitic clays, akageneite, and magnetite (McLennan et al., 2014; Siebach et al., 2014; Léveillé et al., 2014). Features more pervasive along the rover traverse include concretions and relief enhanced features that are sometimes associated with Mg- and Ca-sulfate (Stack et al., 2014; VanBommel et al., 2016; Nachon et al., 2017; Sun et al., 2019), with one ChemCam point on a nodular feature being consistent with jarosite (Nachon et al., 2017). Both the fracture-filled raised ridges and concretions likely formed after the rocks were at least partially lithified but before the formation of the light-toned veins that often cross-cut these features.

Extensive networks of light-toned veins and fracture-associated alteration halos suggest that diagenetic fluids continued to circulate through the rocks for some time after lithification (e.g., Nachon et al., 2014, 2017; Frydenvang et al., 2017; Yen et al., 2017; Gabriel et al., 2019; Kronyak et al., 2019). The APXS and ChemCam instruments have been used to determine the compositions of millimeter- to centimeter-scale light-toned veins and demonstrate that these features are most often Ca-sulfates (Nachon et al., 2014, 2017; VanBommel et al., 2017; Kronyak et al., 2019). APXS measurements show that the ~50 cm wide fracture-associated alteration halos are relatively enriched in SiO<sub>2</sub> and SO<sub>3</sub> compared to the surrounding bedrock, and CheMin analyses indicate these elements are mostly present as high fractions of amorphous silica and sulfates and crystalline Ca-sulfates (Yen et al., 2017). The best constraint on the timing of post-sedimentation fluid interactions is a K-Ar age date < 3 Ga (possibly as young as ~2.1 Ga) for diagenetic jarosite in a single drill hole location (MJ2), indicating that diagenesis continued for a significant amount of time after sedimentation ceased (Martin et al., 2017).

## 2.2 Sulfur-bearing Phase Detection with MSL Instrumentation

CheMin, APXS, and SAM are three of the main instruments onboard MSL capable of detecting and differentiating between sulfur-bearing phases; each has different abundance and phase detection limits. CheMin can detect most crystalline sulfur-bearing phases expected for Gale crater if they are present in abundances > ~1 wt% (Blake et al., 2012). Any crystalline sulfur-bearing phase present below that amount would be automatically allocated to the X-ray amorphous composition, largely because at this abundance, phases lack prominent peaks in the XRD patterns.

APXS measures elemental abundances and can detect SO<sub>3</sub> present in abundances > 0.2 wt%, as well as elements commonly associated with sulfur, such as Ca, Fe, and Mg present at abundances > 0.2, 0.03, and 1 wt%, respectively (Gellert et al., 2015). S-bearing phases can be inferred from correlations between sulfur and cations (e.g., McLennan et al., 2014; VanBommel et al., 2016; Berger et al., 2020). APXS is assumed to measure SO<sub>3</sub> associated with both crystalline and X-ray amorphous sulfur-bearing phases.

SAM has sensitivity for SO<sub>2</sub> at the ppm scale (Mahaffy et al., 2012), and there are no known constraints on the degree of crystallinity of materials that are detectable by SAM (e.g., McAdam et al., 2014). SO<sub>2</sub> gas is evolved from volatile-bearing phases (e.g., minerals and organic molecules) at characteristic temperatures, and so detectability is mostly driven by whether or not a phase decomposes within the temperature range at which the SAM instrument operates (ambient to 900°C; Mahaffy et al., 2012). Phases known to evolve SO<sub>2</sub> in the temperature ranges examined by SAM include elemental sulfur and sulfonic acids, Fe-sulfates and sulfides, Mg-sulfates, and Ca sulfites (Franz et al., 2017). Fe and Mg sulfites have not yet been investigated in SAM-like conditions, but it is likely that they also decompose in the SAM temperature range. Elemental sulfur, sulfonic acids, and Fe sulfides that are oxidized during pyrolysis decompose at temperatures between ~125 and 400°C, Fe-sulfates and sulfides generally decompose at temperatures between ~400 and 700°C, Mg-sulfates decompose at temperatures between ~700 and 900°C, and Ca sulfites decompose at temperatures between ~750 and 850°C (McAdam et al., 2014; Franz et al., 2017; Sutter et al., 2017). Ca-sulfates mostly decompose at temperatures beyond the upper temperature limit for SAM and thus cannot be detected by SAM (e.g., Mu and Perlmutter, 1981; McAdam et al., 2014). However, some phases expected for the Martian surface, such as Ca-, Mg-, and Fe-perchlorates, can catalyze the decomposition of crystalline Ca-sulfates so that Ca-sulfates could have SO<sub>2</sub> peak initiation temperatures ~600°C in the temperature range of SAM; However, the catalyzed Ca-sulfates do not fully decompose within SAM's temperature range (e.g., McAdam et al., 2016).

Few studies have examined EGA SO<sub>2</sub> traces for amorphous, poorly crystalline, and/or nanocrystalline sulfates. McAdam et al. (2014) showed that amorphous ferric sulfate has an EGA SO<sub>2</sub> trace nearly identical to that of crystalline ferric sulfate. Though they did not study sulfates, Archer et al. (2013) showed that a reduction in particle size for calcite lowered the peak decomposition temperature by ~200°C (Archer et al., 2013). These studies suggest that amorphous, poorly crystalline, and/or nanocrystalline sulfates may evolve SO<sub>2</sub> at temperatures approximately equal to or lower than (up to ~200°C lower) those of  $\mu\text{m}$  to mm sized particles. Therefore, if present in Gale crater rocks, amorphous, poorly crystalline, and nanocrystalline Ca-sulfates would still likely evolve SO<sub>2</sub> outside the range measured by SAM, while amorphous, poorly crystalline, and nanocrystalline Mg and Fe-sulfates should be detectable. It is not known if catalysts will also reduce Ca-sulfate's SO<sub>2</sub> peak initiation temperature if the Ca-sulfate is amorphous.

### 3 Methods:

#### 3.1. Mass Balance Approach

This study uses the results of Smith et al. (2021), who calculated bulk X-ray amorphous component compositions for all rock samples through Vera Rubin ridge (VRR; up to sol 2300) and reported X-ray amorphous FeO<sub>T</sub> and SiO<sub>2</sub> contents. The methods from that study are summarized here.

Bulk X-ray amorphous component compositions are estimated through mass balance models. First, XRD-derived minerals and abundances from CheMin are converted to a bulk crystalline component composition. Then, assuming APXS measurements of drill samples represent the bulk sample geochemistry (crystalline + X-ray amorphous), the crystalline component composition is subtracted from the bulk composition, and the residual represents the bulk X-ray amorphous component composition, with the uncertainties listed below. Since APXS



frequently acquires multiple compositions of drill samples (e.g., undisturbed rock, drill tailings, discard pile), Smith et al. (2021) used the same APXS measurements from previous calculations, where applicable, and otherwise averaged compositions from multiple APXS measurements (Table DR3). It should be noted that recommended APXS composition results for the drill sites covered in this study are presented in Berger et al. (2020), published after the calculations were performed for Smith et al. (2021), and in some cases the recommended compositions are different from those used by Smith et al. (2021) (Table DR3). Mineral abundances and compositions were from the published literature (Morrison et al., 2018; Achilles et al., 2020; Rampe et al., 2020b) and are summarized in the Supplemental Material for Smith et al. (2021).

Uncertainties in bulk X-ray amorphous component compositions result from the following caveats and assumptions made for these calculations, discussed in detail in Dehouck et al. (2014) unless otherwise noted: (1) compositions of crystalline phases that might be present below the detection limit of CheMin XRD (~1 wt%) are allocated to the X-ray amorphous component composition by default; (2) minor elemental substitutions in crystalline minerals (e.g., Ti, Mn, Cr, P) not detectable by XRD are also allocated to the X-ray amorphous component composition; (3) when present, poorly constrained clay mineral compositions make it difficult to precisely determine the X-ray amorphous component composition; for samples with ~25 wt% phyllosilicates in the crystalline component, different plausible clay compositions result in differences of  $\leq \sim 2$  wt% CaO, MgO, and FeO<sub>T</sub> in the X-ray amorphous components (Dehouck et al., 2014); (4) uncertainties in CheMin-derived mineral abundances from standard errors and differences in fitting efforts (Morrison et al., 2018; see also Supplemental Material) create a range of possible crystalline component compositions, which results in a range of possible X-ray amorphous component compositions; Smith et al. (2021) calculated a “best estimate” composition for each X-ray amorphous component using the reported mineral abundances from CheMin (i.e., did not consider mineral uncertainties) as well as a range of X-ray amorphous component compositions using the mineral abundance uncertainties. The minimum and maximum X-ray amorphous SO<sub>3</sub> contents for each sample varied on average by 21% of the reported “best estimate” value (Table DR2); (5) the general accuracy of quantitative XRD analytical results for multiphase mixtures is dependent on a great number of factors (e.g., modeling method, background models, accuracy of phase identification, etc.) and is a continuous area of research with a complicated discussion that is beyond the scope of this paper. We mention this here even though the error cannot be quantified, and note that for a given Mars analog sample, both methods employed by the CheMin team (Rietveld refinement and FULLPAT) produce similar mineralogy results, and therefore similar X-ray amorphous component compositions for Mars analog samples (Smith et al., 2018); (6) there are uncertainties on the oxide abundances from APXS measurements detailed in Gellert and Clark (2015) with a relative uncertainty of 15% for SO<sub>3</sub> (see Table DR3 for the errors on each oxide abundance); (7) the new Feed-Extended Drilling/Feed-Extended Sample Transfer (FED/FEST) drilling technique does not allow drill fines to be homogenized in the Collection and Handling for In-Situ Martian Rock Analysis (CHIMRA) device before delivery to CheMin (Rampe et al., 2020a), which complicates the assumption that CheMin and APXS measure the same sample. The first drill site after the anomaly was Duluth (DU) and so this uncertainty is mostly an issue for samples from Duluth (DU) on. Some of these sources of uncertainty can be quantified and we propagate errors to give a minimum error on X-ray amorphous component compositions (calculations described in the Supplemental Text).

### 3.2. SAM Evolved SO<sub>2</sub> trace analyses

To investigate the X-ray amorphous S-bearing phase compositions determined from the mass balance calculations, we report SAM SO<sub>2</sub> evolved gas analysis (EGA) results for five of the nineteen samples in this study (CH, BS1, GH1, MJ2, and WJ; SAM sometimes measures a sample more than once and so the numbers indicate the subsample; Sutter et al., 2017). These five samples were primarily selected because they have relatively high X-ray amorphous SO<sub>3</sub> contents based on the mass balance calculation results. Two of the samples were selected to examine potential differences between X-ray amorphous sulfur compositions in parent Siccar Point rocks (BS) and alteration halos (GH) formed through late-stage diagenetic fluid alteration. The other three samples were selected because the peak fitting methods described below provided results with relatively low uncertainties. Thus, these samples may not be representative of the full suite of X-ray amorphous sulfur-bearing materials compositions at Gale crater.

Volatile content for each sample was determined through pyrolysis of drill fines using the SAM instrument, which consists of a quadrupole mass spectrometer (QMS), gas chromatograph (GC), and tunable laser spectrometer (TLS) (Mahaffy et al., 2012). Samples were heated from ~40°C to ~870 or 900°C (depending on the sample) at a rate of 35°C/min (Sutter et al., 2017; McAdam et al., 2020). Evolved sample SO<sub>2</sub> gas was directly monitored by the QMS resulting in signal versus temperature curves referred to as EGA traces. Evolved SO<sub>2</sub> gas totals were combined with estimated sample mass deliveries to SAM to calculate evolved gas contents (e.g., wt %) (Sutter et al., 2017).

To resolve the S-bearing phases and their abundances from SAM data, peaks were fit to the SO<sub>2</sub> EGA traces using the data analysis and graphing software Origin. Peaks were either fit visually or by using the 2<sup>nd</sup> derivative technique to locate peaks that are difficult to see. Once the peaks were identified, they were fit with Gaussian (for symmetric peaks) or BiGaussian (for asymmetric peaks) curves. The peaks were assigned to phases (e.g., Mg-S, Fe-S) and the areas under the peaks were used to determine the abundances of the phases in each sample. In four of the five samples (CH, GH1, BS1, WJ), one modeled peak fell within the temperature ranges shared by both Mg-S and Fe-S phases (~700°C) and so it could not be determined to which phase the peaks should be attributed (Figure S1). For these samples, we calculated a range of phase abundances, first by ignoring the contribution from the “Mg-S or Fe-S” peak altogether, next by attributing the “Mg-S or Fe-S” peak solely to Mg-S phases, and last by attributing the “Mg-S or Fe-S” peak solely to Fe-S phases.

### 3.3. “Difference method” (assumed X-ray amorphous Ca-sulfate quantification)

Assuming SAM can detect all S-bearing phases present in Gale crater except Ca-sulfates, we attribute the difference between SO<sub>3</sub> contents measured by APXS and SAM ( $\Delta\text{SO}_3$ ) to Ca-sulfate (Sutter et al., 2017) and calculate the abundance of amorphous Ca-sulfate for samples with SAM data in the following steps:

- 1)  $\Delta\text{SO}_3 = \text{SO}_3_{\text{APXS}} - \text{SO}_3_{\text{SAM}}$
- 2)  $\text{SO}_3_{\text{amorph Ca-S}} = \Delta\text{SO}_3 - \text{SO}_3_{\text{cryst Ca-S}}$

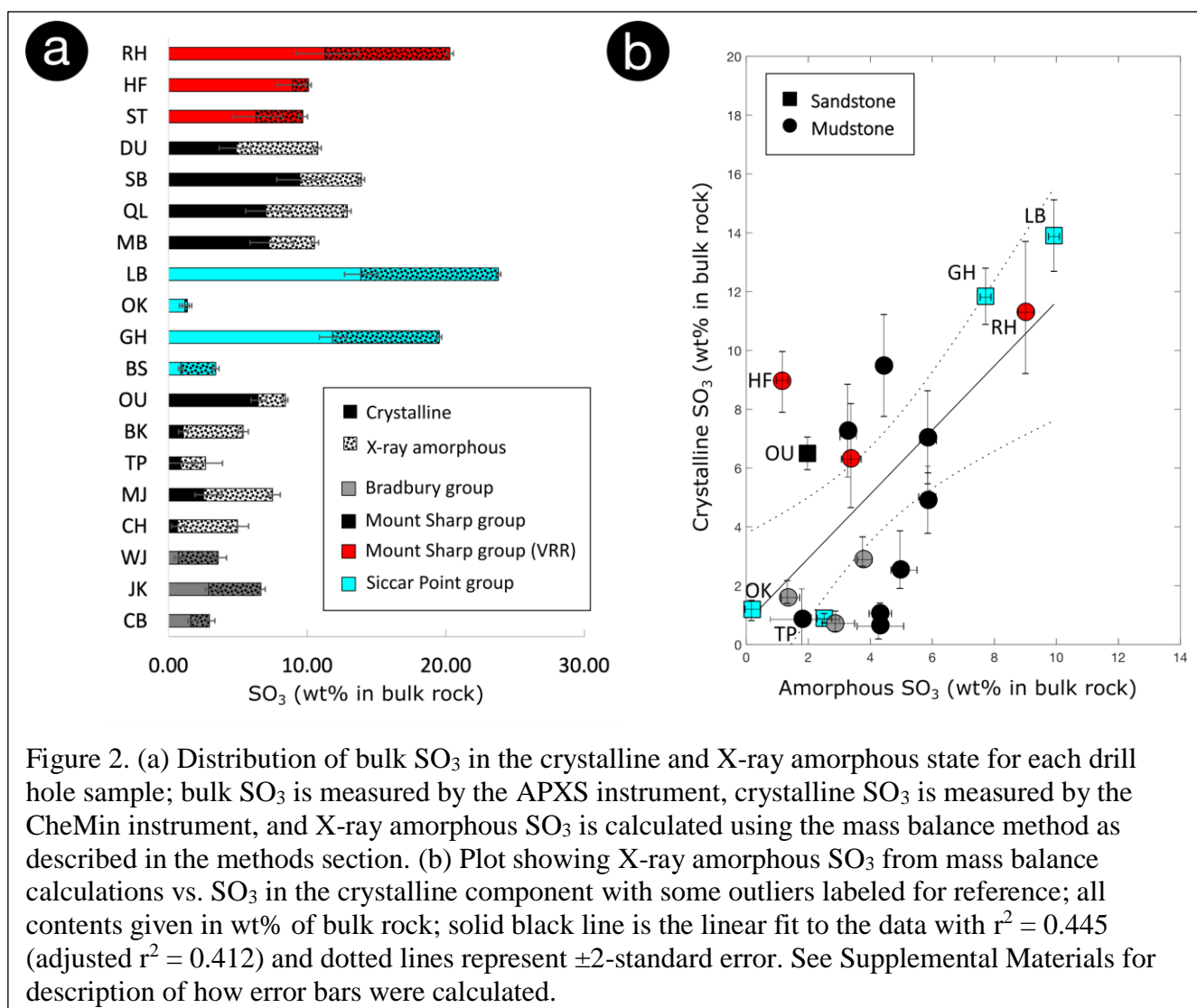
Where  $\text{SO}_3_{\text{APXS}}$  is the bulk SO<sub>3</sub> content (wt%) measured in each sample with the APXS instrument,  $\text{SO}_3_{\text{SAM}}$  is the SO<sub>3</sub> content (wt%) measured in each sample with the SAM instrument,  $\text{SO}_3_{\text{amorph Ca-S}}$  is the abundance (wt%) of amorphous Ca-sulfate in each sample, and  $\text{SO}_3_{\text{cryst Ca-S}}$  is the wt% abundance of SO<sub>3</sub> associated with crystalline Ca-sulfates calculated from CheMin-derived Ca-sulfate abundances. Thus, in the cases where crystalline Ca-sulfates could not account for all the difference between APXS and SAM measurements ( $\Delta\text{SO}_3 - \text{SO}_3_{\text{cryst Ca-S}} >$

0), the remaining  $\text{SO}_3$  was attributed to amorphous Ca-sulfates. Uncertainties associated with this assumption include the fact that SAM  $\text{SO}_3$  abundances are relatively low ( $< 7$  wt%) and can have significant errors associated with the measurements (up to 3 wt%; Table DR5). Additionally, it is possible that some of the difference between APXS and SAM  $\text{SO}_3$  measurements could be attributed to other phases with decomposition temperatures above the SAM range such as, complexes involving  $\text{SO}_3$  adsorbed onto X-ray amorphous alteration products (discussed in greater detail below). Another assumption made in the calculation of the X-ray amorphous material compositions is that APXS, CheMin, and SAM all measure the same material. This is likely an acceptable assumption for the samples with detailed SAM analyses in this study, but is possibly more problematic for sites sampled after the drilling anomaly since drill fines are not homogenized before delivery to CheMin and SAM.

#### 4 Results:

Figure 2a shows the bulk  $\text{SO}_3$  in each rock allocated to the crystalline and X-ray amorphous fractions based on APXS and CheMin data. On average, bulk rocks contain ~5.3 wt% crystalline  $\text{SO}_3$  (standard deviation = 4.4 wt%; range = 0.7 – 14.1 wt%) and ~4.2 wt% amorphous  $\text{SO}_3$  (standard deviation = 2.6 wt%; range = ~0.2 – 9.9 wt%) (Table DR1). Thus, between 20 and 90% of any sample's sulfur content is in the X-ray amorphous state. There is a possible weak correlation between  $\text{SO}_3$  in the crystalline state and  $\text{SO}_3$  in the X-ray amorphous state, with  $r^2=0.25$  (Figure 2b).

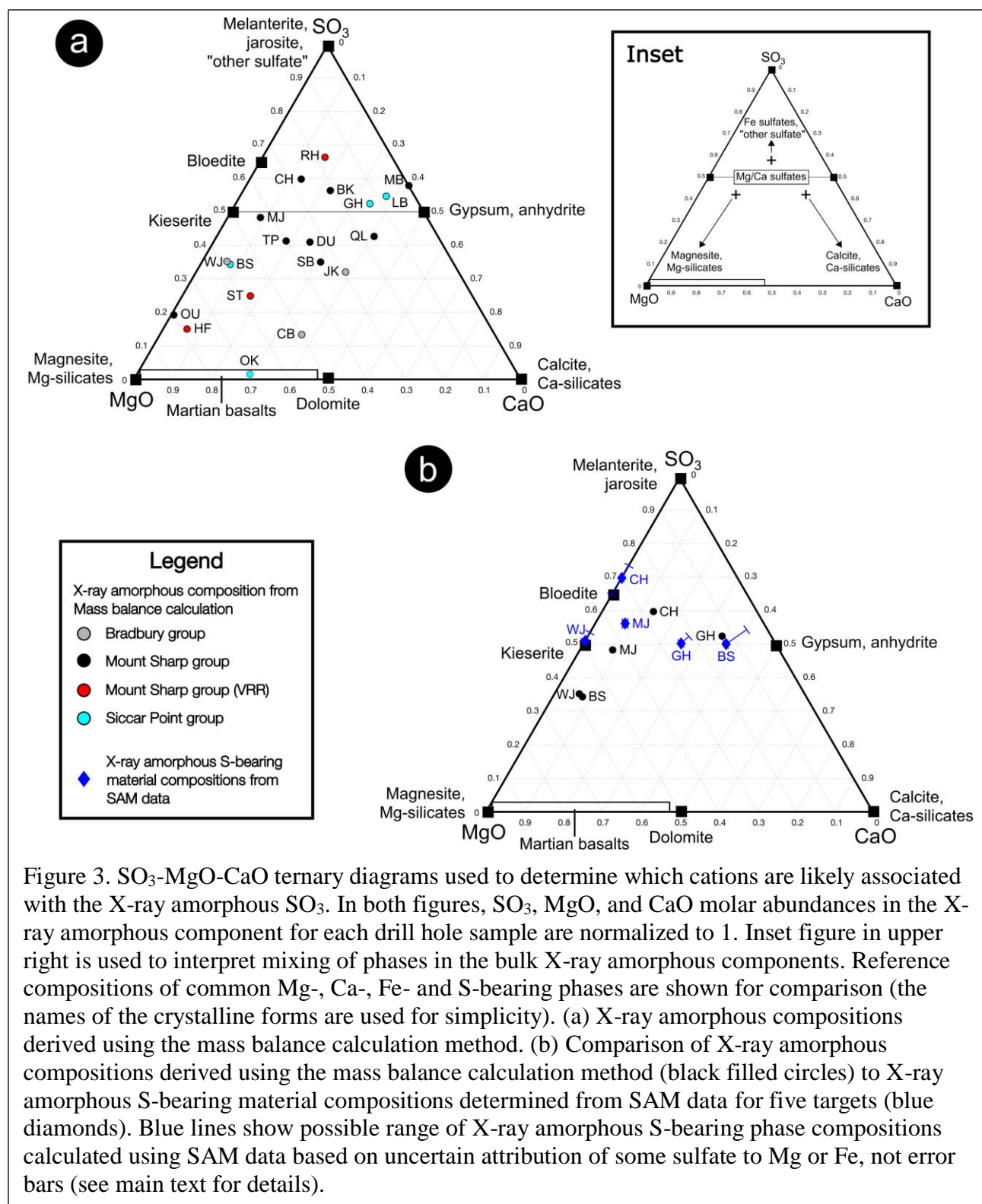
A molar  $\text{SO}_3$ -MgO-CaO ternary diagram (Figure 3a) helps characterize potential compositions of X-ray amorphous sulfur-bearing materials in each drill hole location. In this diagram, the uppermost apex represents Fe-sulfate, as well as any sulfate composition other than Ca or Mg-sulfates (e.g., Al sulfate, Na sulfate, K sulfate, adsorbed  $\text{SO}_3$ , etc.). For this diagram, all sulfur is assumed to be oxidized, and if present, phases such as elemental sulfur and Fe sulfides would plot at the uppermost apex. Any samples with X-ray amorphous compositions that lie above the kieserite—gypsum tie line must have some contribution from those “other” sulfates because they do not have enough amorphous MgO and CaO to balance the amorphous  $\text{SO}_3$ . For these drill hole locations (RH, CH, BK, and MB), we can infer that their X-ray amorphous components represent complex/variable mixtures of X-ray amorphous Ca, Mg, and Fe + “other” sulfates, and possibly mixed cation sulfates. Any sample with an X-ray amorphous component composition that plots below the kieserite—gypsum tie line has more amorphous MgO and/or CaO than amorphous  $\text{SO}_3$ . For these drill hole locations (TP, DU, QL, SB, JK, WJ, BS, ST, OU, HF, and CB), we can infer that their X-ray amorphous components represent complex/variable mixtures of X-ray amorphous Ca, Mg, and Fe + “other” sulfates with other amorphous and poorly crystalline Mg and Ca bearing phases (e.g., silicates). Samples with X-ray amorphous compositions that fall on or close to the kieserite—gypsum tie line have amorphous



408 MgO and CaO that roughly balance the amorphous SO<sub>3</sub>. For these locations (MJ, GH, and LB),  
 409 it is possible that they contain mostly mixtures of Mg and Ca-sulfates (or mixed cation-Ca, Mg-  
 410 sulfates) with essentially no Fe + “other” sulfates.

411 SAM SO<sub>2</sub> EGA trace analysis results are shown in Table 2 and peak fitting models are  
 412 shown in Figure S1. All five samples examined in this study with SAM data show evolved SO<sub>2</sub>  
 413 trace analysis results that indicate some Mg-S. Using the abundance of SO<sub>2</sub> associated with Mg-  
 414 S phases to calculate abundances of X-ray amorphous Mg-sulfates of kieserite composition, we  
 415 find all five samples would have Mg-sulfates at or above the ~1 wt% detection limit of CheMin  
 416 (average = 4.1 wt%; range = 1.0 – 5.6 wt%) (Table DR7) but CheMin did not detect any Mg-S  
 417 phases (Table 1).

418 Likewise, all these samples measured by SAM contain some fraction of Fe-S phases.  
 419 CheMin detected crystalline Fe-S phases in only two of the five samples (CH and MJ2; Table 1),  
 420 and in both cases SAM analysis indicates that these samples contain more SO<sub>3</sub> related to Fe-S  
 421 phases than the CheMin jarosite can account for. Assumptions of either a schwertmannite or  
 422 melanterite composition for the leftover abundance of SAM-measured SO<sub>2</sub> associated with Fe-S



phases produces Fe-sulfates (other than jarosite) at or above the ~1 wt% detection limit of CheMin for these samples (CH and MJ2) (Table DR7). In all samples except Confidence Hills (CH),  $\text{SO}_3$  from X-ray amorphous Mg-S is more abundant than  $\text{SO}_3$  from X-ray amorphous Fe-S,

even when the ambiguous “Fe-S or Mg-S” peaks are attributed to Fe-S phases (Table 2 and Table DR4).

Three of the five samples examined in this study with SAM data (MJ2, BS1 and GH1) do not have enough crystalline Ca-sulfates (“best estimate” abundances) to account for all the difference between APXS and SAM measurements ( $\Delta\text{SO}_3 - \text{SO}_3_{\text{cryst Ca-S}} > 0$ ), and so the remaining  $\text{SO}_3$  was attributed to amorphous Ca-sulfates. Assuming an anhydrite composition for the X-ray amorphous Ca-S phases, we find that these three samples would have Ca-sulfates (other than those already detected) at or above the ~1 wt% detection limit of CheMin (average = 3.2 wt%; range = 1.2 – 5.5 wt%) (Table DR7). Even when the maximum possible Ca-sulfate abundances are taken into account (“best estimate” abundance + 2-sigma uncertainty for each crystalline Ca-sulfate phase), these three samples do not have enough crystalline Ca-sulfates to

**Table 1.** Crystalline sulfur-bearing phases in Gale crater rocks as determined by CheMin analysis.

Sample	CheMin mineralogy				Calculated from CheMin mineralogy	
	Jarosite	Bassanite	Anhydrite	Gypsum	$\text{SO}_3$ (wt%) in crystalline Fe-sulfate	$\text{SO}_3$ (wt%) in crystalline Ca-sulfate
CB	0.0 (0.0)	1.3 (0.1)	0.7 (0.4)	0.0 (0.0)	0.00	1.21
JK	0.0 (0.0)	1.4 (0.1)	2.1 (0.4)	0.0 (0.0)	0.00	2.03
WJ	0.0 (0.0)	0.5 (0.2)	0.5 (0.3)	0.0 (0.0)	0.00	0.58
CH	1.1 (0.7)	0.0 (0.0)	0.0 (0.0)	0.0 (0.0)	0.40	0.00
MJ	3.2 (0.7)	0.0 (0.0)	0.0 (0.0)	0.0 (0.0)	1.14	0.00
TP	1.8 (2.1)	0.0 (0.0)	0.0 (0.0)	0.0 (0.0)	0.63	0.00
BK	0.0 (0.0)	0.0 (0.0)	0.8 (0.2)	0.0 (0.0)	0.00	0.47
OU	0.0 (0.0)	0.0 (0.0)	3.2 (0.6)	2.9 (0.2)	0.00	3.56
MB	0.3 (0.6)	0.8 (1.0)	2.3 (1.4)	1.3 (0.9)	0.12	2.59
QL	0.5 (0.6)	1.9 (0.9)	3.1 (0.7)	0.4 (0.7)	0.18	3.19
SB	0.9 (0.6)	1.1 (0.6)	5.2 (1.6)	1.1 (1.1)	0.32	4.34
DU	0.0 (0.0)	3.3 (0.3)	1.5 (0.5)	0.2 (0.2)	0.00	2.90
ST	1.1 (0.3)	0.5 (0.2)	3.3 (0.3)	2.5 (0.8)	0.39	3.72
HF	0.0 (0.0)	1.2 (0.3)	3.8 (0.5)	2.4 (0.5)	0.00	4.33
RH	2.0 (0.1)	0.0 (0.0)	10.1 (1.5)	0.0 (0.0)	0.72	5.92
BS	0.0 (0.0)	0.0 (0.0)	1.2 (0.2)	0.0 (0.0)	0.00	0.71
GH	0.0 (0.0)	1.4 (0.5)	5.6 (0.5)	0.0 (0.0)	0.00	4.14
OK	0.0 (0.0)	0.8 (0.3)	0.5 (0.3)	0.0 (0.0)	0.00	0.77
LB	0.0 (0.0)	2.4 (0.5)	3.3 (0.5)	0.6 (0.4)	0.00	3.75

Note: all values are wt% in total sample (crystalline + phyllosilicates + X-ray amorphous) and values in parentheses are 2-sigma uncertainties on mineral abundances in %. See Figure 1 caption for full sample name abbreviated here.

**Table 2.** SAM SO<sub>2</sub> EGA trace peak fitting results.

Peak #	Fit	Area (%)	Likely phase	Fe-S <sup>a</sup>	Mg-S <sup>a</sup>
Windjana					
1	Gaussian	2.4 (1.9)	Fe-S		
2	Gaussian	9.3 (0.7)	Fe-S or Mg-S		
3	Gaussian	12.2 (2.7)	Mg-S	0.0	1.0
4	Gaussian	68.7 (6.3)	Mg-S		
5	Bi-Gaussian	7.4 (2.4)	Mg-S		
Confidence Hills					
1	Bigaussian	27.9 (0.9)	Fe-S		
2	Gaussian	18.2 (4.9)	Fe-S		
3	Gaussian	18.7 (1.0)	Fe-S or Mg-S	0.6	0.4
4	Gaussian	27.7 (5.4)	Mg-S		
5	Gaussian	7.5 (1.9)	Mg-S		
Mojave2					
1	Bi-Gaussian	20.3 (2.2)	Fe-S		
2	Bi-Gaussian	4.9 (3.5)	Fe-S		
3	Bi-Gaussian	19.2 (4.3)	Mg-S		
4	Gaussian	12.3 (0.5)	Mg-S	0.3	0.7
5	Gaussian	32.6 (6.7)	Mg-S		
6	Gaussian	4.9 (3.1)	Mg-S		
7	Bi-Gaussian	5.8 (0.9)	Mg-S		
Big Sky (1)					
1	Bigaussian	1.9 (1.3)	Fe-S		
2	Bigaussian	56.7 (3.9)	Fe-S or Mg-S		
3	Bigaussian	11.5 (7.1)	Mg-S	0.0	1.0
4	Bigaussian	25.4 (3.2)	Mg-S		
5	Bigaussian	4.5 (0.8)	Mg-S		
Greenhorn (1)					
1	Gaussian	4.0 (1.2)	Fe-S		
2	Gaussian	13.7 (2.4)	Fe-S or Mg-S		
3	Gaussian	6.5 (0.4)	Mg-S		
4	Gaussian	48.0 (2.4)	Mg-S	0.0	1.0
5	Gaussian	7.0 (2.4)	Mg-S		
6	Bigaussian	20.9 (1.5)	Mg-S		

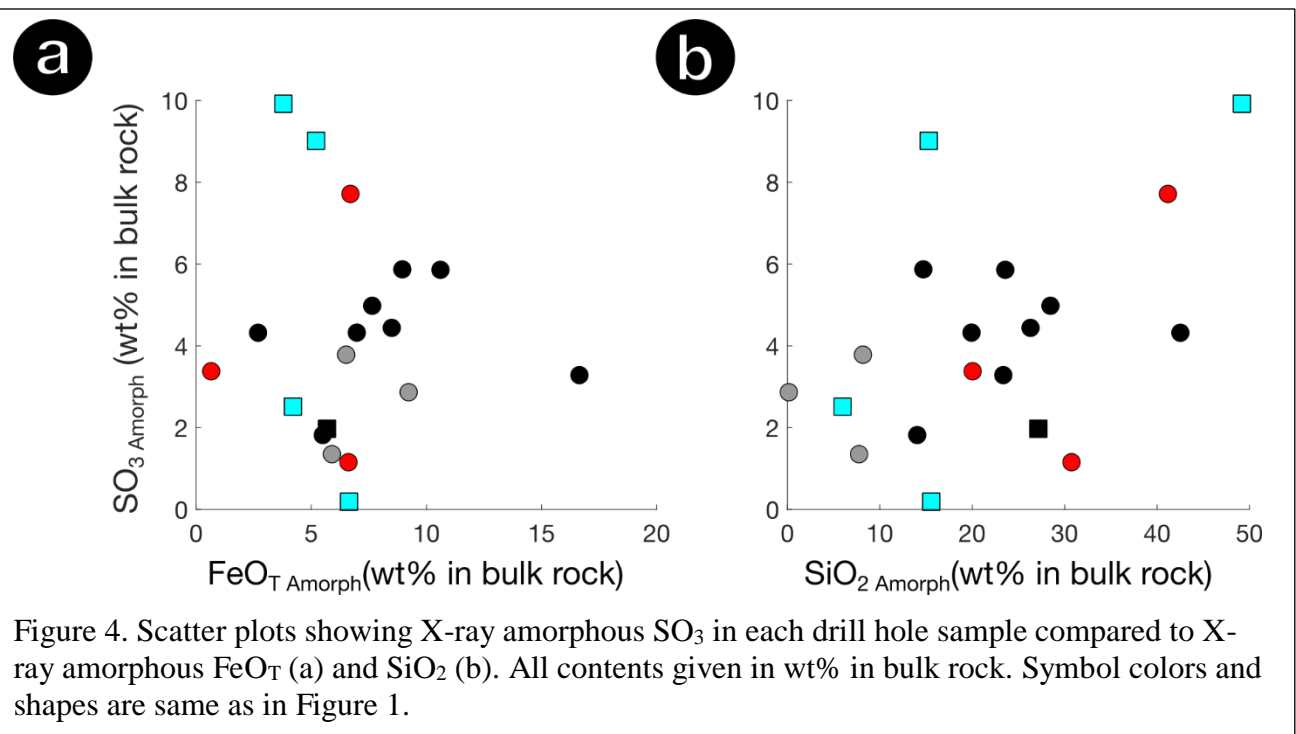
<sup>a</sup>Fraction of phase calculated by ignoring ambiguous peaks. See text in Supplemental for details.

account for all the difference between APXS and SAM measurements ( $\Delta\text{SO}_3 - \text{SO}_3_{\text{cryst Ca-S}} > 0$ ) and the maximum crystalline Ca-sulfate abundances only minimally change the resulting abundances of X-ray amorphous Ca-sulfates (average = 2.8 wt%; range = 1.2 – 4.7 wt%). Additionally, mass balance calculations indicate that these three samples have more moles of X-ray amorphous CaO than moles of SO<sub>3</sub> assumed to be associated with X-ray amorphous Ca-S phases. In other words, assuming a 1:1 molar ratio of SO<sub>3</sub>:CaO, there is always excess X-ray amorphous CaO, implying that the assumed Ca-S associated SO<sub>3</sub> is reasonable and that there are other Ca-bearing X-ray amorphous phases present in these samples.

SAM-derived X-ray amorphous S-bearing compositional ranges were plotted on the same ternary diagram as the mass balance calculation results to determine how well these two

techniques agree (Figure 3b). Ternary plot compositions were calculated for SAM data by combining SAM Mg-S and Fe-S (with crystalline Fe-S phases subtracted) peak integration results with X-ray amorphous Ca-sulfate abundances calculated through equations 1 and 2 (see Supplemental Material for detailed calculation methods). Samples that had relatively large ambiguous “Fe-S or Mg-S” peaks (e.g., BS1) have relatively large compositional ranges that are illustrated by longer blue lines (Figure 3b; blue diamonds show the case where the ambiguous peaks are ignored). Overall, agreement between the mass balance and SAM-derived X-ray amorphous component compositions seems to depend on the X-ray amorphous SO<sub>3</sub> contents. For the samples with relatively high X-ray amorphous SO<sub>3</sub> contents (CH, MJ2 and GH), the X-ray amorphous S-bearing phase compositional ranges calculated using SAM data show reasonable agreement to the X-ray amorphous compositions calculated using the mass balance method. These results indicate that, for these three samples, CaO and MgO in the X-ray amorphous components are likely associated with S-bearing materials (as opposed to silicates, for example). For the samples with relatively low X-ray amorphous SO<sub>3</sub> contents (BS and WJ), there are relatively large differences between the mass balance and SAM-derived compositions, indicating that the X-ray amorphous components for these samples also likely contain significant MgO-bearing phases (e.g., silicates). Because it is difficult to separate cation associations with sulfur vs. other materials such as silicates, we urge significant caution when using mass balance calculation results to infer amorphous sulfate compositions, and recommend performing detailed SAM SO<sub>2</sub> trace analyses.

Even for samples with relatively high X-ray amorphous SO<sub>3</sub> contents, there are some discrepancies between the compositions of X-ray amorphous sulfates in each sample based on SAM and mass balance calculation results. For example, the Greenhorn (GH) and Confidence Hills (CH) samples have more Mg-rich SAM-derived X-ray amorphous sulfur-bearing phase compositions, while the mass balance calculation results would indicate that the X-ray amorphous sulfur-bearing phases are more Ca-sulfate-rich (Figure 3b). It is possible that some of





the SAM-derived SO<sub>2</sub> attributed to Mg-S phases could, in part, come from the catalyzed decomposition of crystalline or amorphous Ca-sulfates. Indeed, these two samples show particularly high-temperature peaks in the evolved SO<sub>2</sub> release traces that are consistent with catalyzed Mg-sulfate and Ca-sulfate phases (Franz et al., 2017). However, they also have relatively low to moderate abundances of evolved O<sub>2</sub> attributed to perchlorate (a possible catalyst) when compared to other samples (Sutter et al., 2017). Perhaps in addition to small amounts of catalyzed Ca-sulfates, this discrepancy could also result from uncertainties in the bulk X-ray amorphous component compositions due to uncertainties in mineral compositions and abundances.

Overall, both the mass balance compositions and the SAM data indicate that the X-ray amorphous S-bearing material in most Gale crater rocks likely consists of complex/variable mixtures of Mg-S, Fe-S, and possibly Ca-S phases. There is no strong trend in X-ray amorphous S-bearing material composition with stratigraphic group (Figure 3a). However, the Siccar Point samples with detectable X-ray amorphous S-bearing materials (BS, GH, and LB) have a significant fraction of the X-ray amorphous S-bearing material attributed to Ca-S phases whereas most of the non-VRR Mount Sharp group rocks (except OU) have X-ray amorphous components that roughly cluster around the tie line between Mg-S and Ca-S phases.

Calculated X-ray amorphous SO<sub>3</sub> contents are compared to the other two most abundant oxides in the X-ray amorphous components, SiO<sub>2</sub> and FeO<sub>T</sub>, in Figure 4. X-ray amorphous SO<sub>3</sub> shows no correlation with X-ray amorphous FeO<sub>T</sub> content (Figure 4a), and there exists a possible weak positive correlation with X-ray amorphous SiO<sub>2</sub> ( $r^2$  value = 0.235; Figure 4b).

Figure 5 shows stratigraphic variations in SO<sub>3</sub> (wt%) in the X-ray amorphous component for each drill hole location. Each stratigraphic group contains a range of X-ray amorphous SO<sub>3</sub> contents, and there is no systematic change in X-ray amorphous SO<sub>3</sub> contents between stratigraphic groups that otherwise show geochemical evidence for changes in sediment source (e.g., across the Bradbury - Mount Sharp group boundary). The Siccar Point group location Okoruso (OK) has the lowest bulk SO<sub>3</sub> and is the only location to have almost no X-ray amorphous SO<sub>3</sub> (Table DR2). The locations with the greatest X-ray amorphous SO<sub>3</sub> contents are found in the Siccar Point group alteration halos Greenhorn and Lubango (GH and LB) and in the VRR sample Rock Hall (RH).

## 5 Discussion:

### 5.1 Constraining X-ray amorphous sulfur-bearing phases

No single instrument on the rover can distinguish with certainty the nature of the X-ray amorphous sulfur-bearing phases. However, we can combine observations to put some constraints on these phases. All locations examined in this study except Okoruso (OK) have X-ray amorphous SO<sub>3</sub> contents > 1 wt%, and both mass balance calculation and SAM analysis results indicate that the X-ray amorphous SO<sub>3</sub> represents mixtures of Mg-S and Fe-S phases, with likely contributions from Ca-S phases. Other possible contributors include reduced phases, e.g., sulfides or sulfur in glass, that were oxidized during the SAM measurements (McAdam et al., 2014; Sutter et al., 2017), and sulfate anions adsorbed onto X-ray amorphous alteration products (e.g., Rampe et al., 2016). The ratios of these phases likely vary between sampling locations, which is reflected in the varying ratios of Mg-S, Fe-S, and Ca-S phases.

SAM EGA SO<sub>2</sub> traces and sulfur isotope data can be used to indicate the oxidation state of sulfur in sulfur-bearing phases. For most of the samples covered in this study (CB through BS/GH), previous SAM analyses show a wide range of sulfur isotopic compositions (Franz et al., 2017). Two of the samples (CB and OU) have significantly <sup>34</sup>S-depleted isotopic compositions,

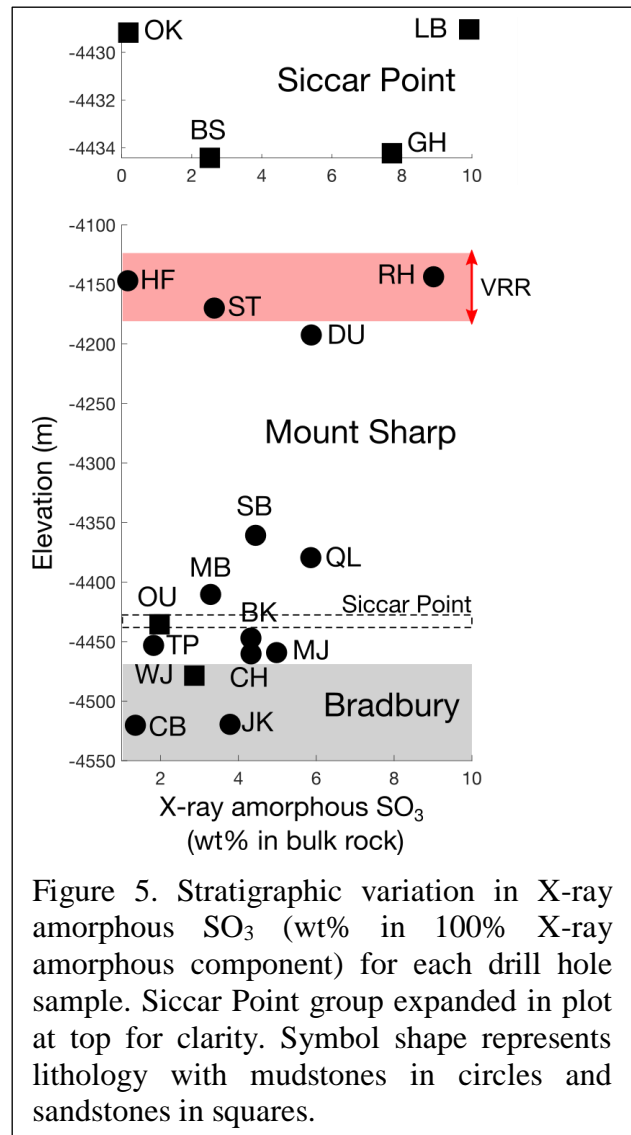


Figure 5. Stratigraphic variation in X-ray amorphous SO<sub>3</sub> (wt% in 100% X-ray amorphous component) for each drill hole sample. Siccar Point group expanded in plot at top for clarity. Symbol shape represents lithology with mudstones in circles and sandstones in squares.

and the SO<sub>2</sub> from these samples was attributed to sedimentary sulfides. Most samples have oxidized S-bearing phases such as sulfates and sulfites, indicating mostly oxidizing conditions during the formation of the X-ray amorphous sulfur-bearing phases.

Potential oxidized S-bearing phases present in the X-ray amorphous components include crystalline sulfates or sulfites present below the detection limit of CheMin (~1 wt%); amorphous, nanocrystalline, or poorly crystalline sulfates and sulfites; and SO<sub>4</sub><sup>2-</sup> anions adsorbed onto X-ray amorphous alteration products. Due to instrument limitations, we are unable to definitively determine the crystallinity of the S-bearing phases that make up the X-ray amorphous fraction. In four of the five samples for which we have SAM peak integrations (WJ, CH, MJ2, and GH1), SAM-derived SO<sub>3</sub> associated with Mg-S phases is > 1 wt%, which should be detectable by CheMin if these contents represented a single crystalline Mg-S phase. The fact that they are not detected by CheMin indicates that either this material is amorphous, nanocrystalline, or poorly crystalline or there are multiple crystalline Mg-S phases each present at < ~1 wt%. The same can be said for SAM-derived SO<sub>3</sub> associated with Fe-S phases where present above the detection limit of CheMin. Below we discuss these possibilities.

Amorphous, poorly crystalline, and nanocrystalline sulfates have been previously hypothesized for the Martian surface as the current cold and dry environmental conditions are conducive to the formation and preservation of these phases. Amorphous sulfate solids can form through two general means: (1) direct precipitation or (2) structural destabilization of previously crystalline sulfates. Research over the past few decades has shown that most crystalline phases formed at low temperatures have amorphous and nanocrystalline precursors, and Ca-sulfates such as gypsum are no exception (e.g., Wang, Y. et al., 2012; Jia et al., 2020). However, amorphous calcium sulfates have very short lifetimes in laboratory settings and experiments generally produce small quantities (e.g., Wang, Y. et al., 2012; Morris et al., 2015). Morris et al. (2015) found that freeze-drying mixed cation sulfate solutions (e.g., Fe<sup>3+</sup>, Mg<sup>2+</sup>, Na<sup>+</sup>, K<sup>+</sup>) will cryoprecipitate XRD detectable abundances of amorphous sulfates but freeze-drying single cation sulfate solutions (Ca<sup>2+</sup>, K<sup>+</sup>, Na<sup>+</sup>) will not. The complexity of X-ray amorphous sulfur-phase compositions in Gale crater suggest mixed cation solution compositions that might have precipitated greater abundances of amorphous (vs. crystalline) precipitates. However, possibly more likely for Gale crater is the formation of amorphous, poorly crystalline, and nanocrystalline sulfates when hydrated crystalline sulfates experience rapid dehydration, which causes structural destabilization. This has been shown to be an important process for hydrated Mg and Fe-sulfates and could take place upon exposure to surface conditions during erosion or upon exposure to warmer and drier conditions inside the rover instruments during sample measurement (Vaniman et al., 2004; Vaniman and Chipera, 2006; Wang et al., 2009; Wang and Zhou, 2014; Sklute et al., 2015, 2018). However, while gypsum could dehydrate to bassanite and possibly anhydrite under Mars surface conditions (Vaniman et al., 2018), we could find no examples in the literature for the formation of amorphous Ca-sulfates through the structural destabilization of hydrated crystalline Ca-sulfates. Therefore, it is uncertain if the X-ray amorphous Ca-S materials in Gale crater rocks could have formed through dehydration. More work is needed to determine if these X-ray amorphous Ca-S phases are truly present and, if they are present, more work is needed to better understand their formation mechanisms.

Sulfate anions can be adsorbed onto X-ray amorphous weathering products, such as allophane and ferrihydrite, in soils on Earth (e.g., Ishiguro et al. 2006) at contents comparable to X-ray amorphous SO<sub>3</sub> contents reported for Gale crater rocks (Jara et al. 2006; Rampe et al.,

2016). These X-ray amorphous weathering product – sulfate complexes would be X-ray amorphous to CheMin if present in Gale crater rocks. Rampe et al. (2016) examined XRD patterns and evolved SO<sub>2</sub> release traces for complexes consisting of sulfate anions chemisorbed onto allophane and ferrihydrite. They found that the sulfate – allophane complex had peak SO<sub>2</sub> releases at temperatures outside the usual temperature range for the SAM instrument, and so this complex would not be detectable by SAM and could be an alternate explanation for the SO<sub>3</sub> interpreted here as amorphous Ca-sulfate. Using the X-ray amorphous Al<sub>2</sub>O<sub>3</sub> contents of the samples in this study with SO<sub>3</sub> attributed to amorphous Ca-sulfate (MJ2, BS1, and GH1), we find that 18.7%, 8.5%, and 0.2% of their respective X-ray amorphous components could be comprised of Al-rich allophane. However, we point out that X-ray amorphous Al<sub>2</sub>O<sub>3</sub> contents and SO<sub>3</sub> attributed to amorphous Ca-sulfate are seemingly anticorrelated in this sample set (e.g., MJ2 has the lowest abundance of potential amorphous Ca-sulfate and highest potential allophane contribution while GH1 has the highest abundance of potential amorphous Ca-sulfate and the lowest potential allophane contribution). Thus, allophane– sulfate complexes could explain some, but probably not all of the amorphous SO<sub>3</sub> attributed to Ca-S. The sulfate – ferrihydrite complex did evolve SO<sub>2</sub> in the temperature range measured by SAM, but the shape of the trace was inconsistent with that from the Rocknest soil and John Klein samples (Rampe et al., 2016), as well as the subsequent drill holes (e.g., CB, WJ, CH, MJ, TP, BK, BS, and GH) (Sutter et al., 2017). Thus, these specific sulfate anion – X-ray amorphous weathering product complexes are not likely major contributors to the X-ray amorphous SO<sub>3</sub> components in Gale crater rocks, but it is possible that other adsorbed sulfate - X-ray amorphous weathering product complexes are present, given the wide range of X-ray amorphous weathering products found in terrestrial analog sedimentary materials (Smith and Horgan, 2021).

Terrestrial settings are known to have a plethora of crystalline Mg and Fe-sulfate and hydrated sulfate phases, and sulfate phase assemblages can be complex (Chou et al., 2013 and references therein). Laboratory experiments suggest the same may be true for the Martian surface and subsurface (Chou et al., 2013 and references therein), indicating that multiple crystalline oxidized sulfur-bearing phases could be present below the CheMin detection limit. For instance, there is significant overlap in the temperature and relative humidity stability fields for MgSO<sub>4</sub> • 1H<sub>2</sub>O, MgSO<sub>4</sub> • 4H<sub>2</sub>O, and amorphous MgSO<sub>4</sub> • nH<sub>2</sub>O (Chou et al., 2013), suggesting multiple crystalline hydrates could be present and could also be intimately mixed with amorphous Mg-sulfates.

Possible reduced S-bearing phases contributing to the X-ray amorphous S-bearing material are crystalline sulfide phases present below the detection limit of CheMin and S-bearing inclusions in minerals or glass (McAdam et al., 2014; Sutter et al., 2017). SAM can detect the pyrolysis of reduced sulfur-bearing phases, and some of the samples have at least one SO<sub>2</sub> peak consistent with oxidized elemental sulfur or sulfides (CB and MJ2) (Franz et al., 2017). Petrographic analyses of Martian meteorites show that the Martian crust contains a range of reduced S-bearing phases such as pyrrhotite, rare chalcopyrite and/or cubanite, pentlandite, troilite-pentlandite-chalcopyrite intergrowths, pyrite, and some secondary marcasite (Meyer 2008 and references therein). Collectively, these phases compose a minor component of the Martian crust, with S present at < 1 wt% (equivalent to 2.0 wt% SO<sub>2</sub> and 2.5 wt% SO<sub>3</sub>). Ion microprobe analyses of primitive shergottite meteorites indicate that sulfur is present in mineral-hosted melt inclusions at < ~0.2 wt% (equivalent to 0.4 wt% SO<sub>2</sub> and 0.5 wt% SO<sub>3</sub>) and in groundmass glass at < ~0.6 wt% (equivalent to 1.2 wt% SO<sub>2</sub> and 1.5 wt% SO<sub>3</sub>) (Usui et al., 2012). These observations indicate that oxidation of reduced S-phases in melt inclusions and groundmass glass

could collectively produce up to ~ 1.6 wt% of the SAM evolved SO<sub>2</sub> (~2.0 wt% SO<sub>3</sub>) in any sample. These minor phases could account for the relatively small X-ray amorphous S-bearing material contents of the Cumberland (CB) sample (1.4 wt%) and the small low temperature SO<sub>2</sub> peak for Mojave2 (MJ2), as shown in Franz et al. (2017). Note that if present at these fractions, elemental sulfur and sulfides should be detected by both the SAM and APXS instruments, so these phases cannot explain the ΔSO<sub>3</sub> that we attribute to Ca-S.

## 5.2 Relative timing of deposition

X-ray amorphous SO<sub>3</sub> contents show no strong correlation with either X-ray amorphous SiO<sub>2</sub> or FeO<sub>T</sub>, unlike the anticorrelation observed between X-ray amorphous SiO<sub>2</sub> and FeO<sub>T</sub> contents as reported by Smith et al. (2021). Additionally, X-ray amorphous SO<sub>3</sub> content does not change across the Bradbury Group - Mount Sharp boundary. Previous studies have shown evidence for changes in sediment source (Bedford et al., 2019) and increased chemical alteration (e.g., Mangold et al., 2019) across this boundary, and the observation that X-ray amorphous SiO<sub>2</sub> increased across the boundary was used as evidence to hypothesize that the X-ray amorphous SiO<sub>2</sub> was also linked to the sediment source regions for many Bradbury and Mount Sharp group rocks (Smith et al., 2021). The lack of correlation between X-ray amorphous SO<sub>3</sub> and source regions indicates that X-ray amorphous SO<sub>3</sub> deposition was, for the most part, (i) unrelated to the deposition of X-ray amorphous SiO<sub>2</sub> and FeO<sub>T</sub>, (ii) that SO<sub>3</sub> concentrations were much more variable than SiO<sub>2</sub> in the source rocks or fluids that deposited the X-ray amorphous materials, and/or (iii) that later diagenetic fluids introduced new SO<sub>3</sub> or mobilized and redistributed SO<sub>3</sub>, overprinting any original correlation with the other X-ray amorphous component constituents.

Observations of most of the Bradbury and Mount Sharp group locations covered in this study indicate that late-stage diagenetic fluids were primarily confined to fractures. For the most part, sharp contacts between mineral infilling and host rock indicate that the sediments were well lithified before the formation of the fractures (De Toffoli et al., 2020) and there is no evidence that the sulfur-bearing diagenetic fluids permeated the surrounding bedrock. APXS studies consistently find that vein-bearing targets have CaO:SO<sub>3</sub> weight ratios of ~3:2, consistent with Ca-sulfate (Berger et al., 2020). Additionally, a comparison of measured areas of light-toned veins in the Cumberland and John Klein bore holes with the CheMin Ca-sulfate abundances indicate that most, if not all of the XRD-detected Ca-sulfates at these locations could be associated with such visible diagenetic features (e.g., Vaniman et al. 2014). Thus, if the X-ray amorphous S-bearing materials reside in the bedrock, as is likely since there is no indication of large, continuous salt deposits (Rapin et al., 2019), the simplest conclusion is that the X-ray amorphous S-bearing materials were deposited before the diagenetic veins. Fractures and diagenetic veins are interpreted to have formed mostly during late diagenesis (post cementation) (e.g., Nachon et al., 2014, 2017; Rapin et al., 2016; Kronyak et al., 2019; De Toffoli et al., 2020) and so the X-ray amorphous SO<sub>3</sub> would have been deposited either with the detrital sediments (syn-depositional) or during early diagenesis, possibly contributing to sediment cementation.

Sulfate cements have been hypothesized for Gale crater rocks in previous studies (e.g., Blaney et al., 2014; Newsom et al., 2016; Rapin et al., 2019). APXS measurements have shown many instances where Gale crater bedrock has SO<sub>3</sub>:CaO ratios that trend away from the simple addition of Ca-sulfate, indicating the presence of other cation sulfur-bearing phases (Berger et al., 2020). Dendritic and spherical concretions (cemented features) often show a positive correlation between MgO and SO<sub>3</sub> and could be enriched with ~10-15 wt% pure MgSO<sub>4</sub>

(VanBommel et al., 2016, 2017). Thus, Berger et al. (2020) hypothesized that some Mg-sulfate could also be present in the bedrock matrix, likely at abundances equal to or lower than Mg-sulfate in the concretions, which is consistent with bedrock Mg-sulfate abundances determined in this study. While the ChemCam LIBS instrument does not quantify volatiles (e.g., S, H, C and P) directly, their presence can be inferred from low oxide totals that indicate “missing components” and peaks in the LIBS spectra (see Nachon et al., 2014 for an in-depth discussion). ChemCam data were used to hypothesize the presence of impure Ca-sulfate cements for sections of the Missoula interval, which belongs to the Stimson formation in the Siccar Point group (Newsom et al., 2016). The Missoula member was not sampled by CheMin, and so there is no information about the crystallinity of the ChemCam-detected Ca-sulfate cement. The nearest unaltered Stimson drill hole locations are Okoruso (OK) and Big Sky (BS), which were sampled at a slightly higher elevation in the Stimson formation. Okoruso has negligible X-ray amorphous SO<sub>3</sub>, but SAM analyses indicate that Big Sky has a significant X-ray amorphous Ca-sulfate component that could be consistent with the ChemCam observations. Rapin et al. (2019) also used ChemCam data to show evidence for Ca-sulfate-enriched bedrock in the Sutton Island and Blunts Point members of the Murray formation, with a ~10 m-thick section of possibly Mg-sulfate-enriched bedrock in the Sutton Island member. The base of the Sutton Island member was sampled at Sebina (SB) and the upper section of the Blunts Point member was sampled at Duluth (DU); both samples have X-ray amorphous component compositions that lie relatively close to the tie-line between kieserite and gypsum on the ternary diagram in Figure 3a, and could be consistent with ChemCam observations of Ca- and Mg-sulfate cements. However, the enrichments estimated by Rapin et al. (2019) (30-50 wt% Ca-sulfate and ~25 wt% Mg-sulfate) far exceed X-ray amorphous Ca and Mg-sulfate values estimated for Sebina and Duluth drill holes in this study (0-5.5 wt% and 1-5.5 wt%, respectively; Table DR6). This discrepancy could possibly be a result of the distance between the sites observed with ChemCam and the drill sites.

Late diagenetic overprinting has been observed in multiple locations along the rover traverse (discussed in Section 2.1, above), and the samples from these locations have some of the highest and lowest X-ray amorphous SO<sub>3</sub> contents. For example, the two drill hole locations that represent the light-toned, silica-rich alteration “halos” sampled in the Siccar Point group (LB and GH) have some of the highest X-ray amorphous (this study) and crystalline SO<sub>3</sub> contents (Yen et al., 2017) observed. Additionally, the results from our study suggest that the X-ray amorphous and crystalline sulfur-bearing phases in the alteration halos have similar compositions, both being Ca-sulfate-rich. It is unclear how the crystalline and X-ray amorphous S-bearing phases in the alteration halos are related, if at all. Do their similar compositions indicate that crystalline Ca-sulfate deposited during late diagenesis was later partially altered to become X-ray amorphous or that the X-ray amorphous Ca-sulfates represent amorphous precursors that have yet to be converted to more crystalline phases? Interestingly, our SAM data analyses suggest that the composition of the X-ray amorphous S-bearing material in the unaltered bedrock surrounding the halos (BS) is also predominantly Ca-sulfate. The relationship, if any, between the X-ray amorphous S-bearing material in the host rock and the alteration halos remains unclear. The Siccar Point group rocks are sandstones (Banham et al., 2018) and are likely relatively permeable, so it is possible that halo-forming late-diagenetic fluids infiltrated the surrounding bedrock to precipitate the X-ray amorphous Ca-sulfate.

Some VRR locations also have strong evidence for late-stage diagenetic overprinting. The Rock Hall (RH) and Highfield (HF) samples represent portions of VRR bedrock that display “red” and “grey” coloring, respectively. The difference in coloring has been attributed to

differences in hematite grain size stemming from differences in diagenetic fluid interactions, with red colors resulting from the syn-depositional or early diagenetic formation of fine-grained ferric species, and the gray colors resulting from late-stage diagenetic alteration by groundwater to coarser-grained iron species (e.g., L'Haridon et al., 2020). As such, the Highfield location is thought to have experienced more late-stage diagenetic alteration, and so the low X-ray amorphous SO<sub>3</sub> contents could have resulted from the removal or recrystallization of any X-ray amorphous SO<sub>3</sub>, or could suggest that the VRR late-stage diagenetic fluids were less sulfur-bearing than the fluids that formed the alteration “halos” in the Siccar Point group. In contrast, the Rock Hall sample has high X-ray amorphous SO<sub>3</sub> contents that are comparable to those in the Siccar Point group alteration “halos” and has very high abundances of crystalline Ca-sulfates (anhydrite) and minor jarosite (Rampe et al., 2020b), all of which indicate sulfur-rich fluid interactions at this VRR location at one point in time. These X-ray amorphous SO<sub>3</sub> observations are further evidence for spatially variable mobilization and redeposition of geochemical components with diagenetic fluid activity within Gale crater.

### 5.3 Consequences for Gale crater environmental conditions

Mass balance calculation results coupled with SAM SO<sub>2</sub> EGA trace analyses indicate that in most cases, X-ray amorphous S-bearing materials are complex/intimate mixtures of Mg-S, Fe-S, and possibly Ca-S phases that are likely oxidized (sulfates or sulfites) with reduced S phases as possible low-level contributors. If these X-ray amorphous S-bearing materials are aqueously deposited sulfates and sulfites, what implications do they have for the compositions of fluids in Gale crater? Additionally, if they are amorphous, nanocrystalline, and/or poorly crystalline sulfates, what can these materials tell us about post-depositional environmental conditions?

A hypothesis for the formation of sulfate and sulfite evaporite deposits in Gale crater sedimentary rocks involves the concentration and evaporation of brines derived from basaltic weathering during early diagenesis (Rapin et al., 2019). Terrestrial studies show that an important parameter responsible for brine compositions and evaporite mineral assemblages is the composition of the dilute water at the onset of concentration (Hardie and Eugster, 1970). The mostly basaltic crust of Mars coupled with high sulfur contents would produce fluids rich in Mg, Ca, Fe (depending on redox conditions and pH), SiO<sub>2</sub>, and SO<sub>3</sub> compared to weathering solutions on Earth (e.g., Burns 1993; Catling 1999; King and McLennan, 2010). Modeling efforts have shown that the evaporite mineralogy precipitated from such Martian weathering solutions would be dominated by Mg, Fe (depending on redox conditions and pH), Ca-sulfates and silica phases such as amorphous silica (Tosca and McLennan, 2006).

Compared to other sulfate assemblages examined in situ on Mars, including crystalline, amorphous, or phases of unknown crystalline state, Gale crater rocks seem to have relatively less Fe-S phases and more Mg-S and Ca-S phases. Crystalline Fe-sulfate (jarosite) was detected in eight of the nineteen drill hole locations examined in this study at ~1-3 wt% in the bulk rock (Table 1; Rampe et al., 2020a), and X-ray amorphous Fe-S phases were found to be relatively significant in two of the five rocks examined in this study using detailed SAM analyses (CH and MJ2). In contrast, the instrument suite of the Opportunity rover determined that the Burns formation of Meridiani Planum consisted of ~10 wt% jarosite (via combined APXS and Mössbauer), ~18 wt% Mg-sulfate, and ~10 wt% Ca-sulfate (via APXS and TIR spectroscopy) (Clark et al., 2005; McLennan and Grotzinger, 2008). Since this study examined only a small subset of samples with detailed SAM analyses, it is unclear how important amorphous Fe-S

phases are in Gale crater rocks. Future studies with larger sample sets are necessary to better determine the spatial and temporal variability of crystalline and amorphous Mg, Fe, and Ca phase ratios below and through the mineral transition. Such work can help constrain changes in environmental conditions in Gale crater that can be compared to other rover landing sites.

The relative rarity of crystalline or X-ray amorphous Fe-S at some Gale crater drill hole locations (e.g., WJ, BS and GH) could be a result of environmental factors (pH, temperature) and/or parent rock lithology different from other locations on Mars. Ferric and ferrous iron sulfates, such as jarosite and melanterite, typically form in acidic environments on Earth (e.g., Cogram, 2018). For example, at 298 K, jarosite is stable between pH ~2.5 to 3.5 under oxidizing conditions (e.g., Elwood Madden et al., 2004). Tosca et al. (2005) modeled evaporite assemblages of different weathering fluids relevant for Mars and showed that weathering fluids with pH > 3.5 will not produce jarosite, and at slightly higher pH levels, fluids will precipitate the poorly crystalline Fe-hydroxysulfate schwertmannite (pH ~2.5-6) (Tosca et al., 2005). Thus, the lack of both crystalline and X-ray amorphous Fe-S phases at these locations could indicate a near-neutral fluid pH (> ~6). Alternatively, weathering solutions could have been more acidic, initially precipitating jarosite, but with continued diagenetic fluid interactions, jarosite would eventually breakdown to form goethite (Tosca et al., 2005). No goethite has been detected at any of the drill hole locations in this study, but goethite can alter over time with continued diagenetic fluid interactions to form hematite. However, this seems to be an unlikely pathway for Gale crater as continued diagenetic fluid interactions would also likely have recrystallized the amorphous SiO<sub>2</sub> and FeO<sub>T</sub> phases found in high abundance in nearly all drill hole locations (Smith et al., 2021).

An alternative explanation for the presence of X-ray amorphous S-bearing phases in the bedrock (as opposed to having been precipitated from weathering fluids during early diagenesis) is their emplacement by brines originating from the overlying sulfate-bearing unit that is detected from orbit. Bristow et al. (2021) argue that the emplacement of the aerially extensive and thick sulfate-bearing unit would have caused density-driven brine infiltration into the underlying Mount Sharp group sediments prior to lithification. The brines would have been silica-poor, which could have promoted the destabilization of detrital feldspar and Fe-bearing clay minerals, forming X-ray amorphous silica and iron-bearing materials and depositing Mg and Ca-sulfates (Bristow et al., 2021).

Materials originally precipitated as amorphous should easily dissolve or recrystallize into crystalline materials with time, heat, and water, and this would especially be the case for such soluble phases as sulfates. In fact, laboratory crystallization experiments have shown that amorphous Ca-sulfate precursors form faceted gypsum crystals after ~40 minutes at 90°C (Jia et al., 2021). Thus, it would be very surprising if these are primary (~3-4 Ga) materials that stayed amorphous during burial in Gale crater. More likely, these X-ray amorphous phases represent multiple crystalline S-bearing phases each present below the detection limit of CheMin or phases that more recently became amorphous through partial dehydration, as has been shown to happen for epsomite (Vaniman et al., 2004; Vaniman and Chipera, 2006; Wang et al., 2009) and hydrated Fe-sulfates (Wang and Zhou, 2014; Sklute et al., 2015, 2018). Hydrous evaporative phases initially deposited as crystalline could have become amorphized when exposed through erosion to surface conditions or by the rover to instrument conditions.



Regardless of crystallinity, Mg-sulfates are the most soluble of the three mono-cation sulfates considered here (Ca, Mg, and Fe-sulfates), and any post-depositional interactions with dilute meteoric surface or ground waters would have caused preferential dissolution of the Mg-sulfates. Because of their solubility, the fact that the X-ray amorphous S-bearing components of many Mount Sharp group rocks are seemingly dominated by Mg-sulfates suggests negligible fluid flow through the bulk bedrock post-Mg-sulfate deposition at these locations. It should be noted that the presence of 2.1 Ga jarosite in the Mojave2 bedrock sample (Martin et al., 2017), which also contains a large fraction of X-ray amorphous Mg-S phases, indicates some fluid interactions long past sediment lithification. The question is whether or not this jarosite is representative of more pervasive late diagenetic fluids infiltrating bedrock throughout Gale crater or if it formed through very localized reactions. The fact that jarosite is not detected in more drill sites is an argument in support of more localized processes.

## 6 Implications

Hydrated amorphous sulfates have visible and near infrared (VNIR) spectral features at the same positions as their crystalline counterparts (Wang, A. et al., 2009), and so the crystalline state of hydrated Mg-sulfates detected from orbit cannot be discerned. Spectral maps from Milliken et al. (2010), Fraeman et al. (2016) and Sheppard et al., (2021a) show that most of the rocks traversed by the rover through sol 2300 have been spectrally bland, have shown phyllosilicate spectral signatures mixed with weak hydrated Mg-sulfate spectral signatures, or have been consistent with mafic minerals that might have obscured or weakened sulfate spectral signatures. This study used in situ investigations from the Curiosity rover to confirm that the sedimentary rocks of Gale crater from the landing site through VRR contain Mg-S phases, most likely Mg-sulfates intimately mixed with Fe and Ca-sulfates, all of which appear X-ray amorphous to CheMin.

The rocks higher up Mount Sharp in the “sulfate unit” have much stronger hydrated Mg-sulfate spectral signatures and the reasons for the increase in spectral signature strength have yet to be discovered (Milliken et al., 2010; Sheppard et al., 2021a). Several hypotheses regarding this transition can be tested as the rover enters the sulfate unit. One hypothesis is that, regardless of crystalline state, Mg-sulfate contents are higher in the sulfate unit with relatively fewer mafic minerals to mask the sulfate spectral signatures. Such a finding would indicate a more saline or less water-dominated environment. A second hypothesis is that the range of Mg-sulfate contents does not change significantly across the transition, but the sulfate-bearing unit is less dusty, allowing for a stronger bedrock signature to reach the orbiting spectrometer. A third hypothesis is that the range of Mg-sulfate contents does not change significantly across the transition, but there is an increase in crystallinity or hydration state in the sulfate unit resulting from a difference in exposure to Martian surface conditions. The spectral contrast of hydrated sulfates decreases with decreasing crystallinity and hydration, which would make amorphous phases more challenging to detect, especially when present in mixtures with strong absorbers (Sheppard et al., 2021b). Lastly, the presence of > ~10 wt% clay minerals has been shown to obscure the spectral signature of amorphous Mg-sulfates (Sheppard et al., 2021a), and so a fourth hypothesis is that clay minerals are not present (or present at low abundance) in the sulfate unit. Clay minerals have been detected at most drill hole locations in this study, and so a decrease in clay minerals would indicate a major shift in environment, during weathering in the source region or during diagenesis, depending on whether the clay minerals are detrital or diagenetic (Bridges et al., 2015; Bristow et al., 2018), or could also possibly indicate the destruction of once present

clay minerals through diagenetic alteration (Bristow et al., 2021). Testing these hypotheses will be important for understanding the evolution of the Martian surface environment and climate at Gale crater.

**Acknowledgments:** There are no real or perceived financial conflicts of interests for any author. All data supporting the conclusions can be obtained within the article and in the referenced published work, or in the Supplemental Material (Smith R., 2021) found here: <http://dx.doi.org/10.17632/8b5yj38wx3.1>. This work was funded through a NASA Participating Scientist award to SMM (JPL Subcontract 1457128). A portion of this research was carried out at the Jet Propulsion Laboratory, California Institute of Technology, under a contract with the National Aeronautics and Space Administration (80NM0018D0004). The authors are indebted to the MSL science, engineering, and management teams for their efforts in tactical and strategic operations.

## References

- Achilles, C. N., Rampe, E. B., Downs, R. T., Bristow, T. F., Ming, D. W., Morris, R. V., Vaniman, D. T., Blake, D. F., et al. (2020). Evidence for Multiple Diagenetic Episodes in Ancient Fluvial-Lacustrine Sedimentary Rocks in Gale Crater, Mars. *Journal of Geophysical Research: Planets*, 125(8). <https://doi.org/10.1029/2019JE006295>
- Archer, P. D., Ming, D. W., & Sutter, B. (2013). The effects of instrument parameters and sample properties on thermal decomposition: Interpreting thermal analysis data from Mars. *Planetary Science*, 2(1), 2. <https://doi.org/10.1186/2191-2521-2-2>
- Banham, S. G., Gupta, S., Rubin, D. M., Watkins, J. A., Sumner, D. Y., Edgett, K. S., Grotzinger, J. P., Lewis, K. W., et al. (2018). Ancient Martian aeolian processes and palaeomorphology reconstructed from the Stimson formation on the lower slope of Aeolis Mons, Gale crater, Mars. *Sedimentology*, 65(4), 993–1042. <https://doi.org/10.1111/sed.12469>
- Bedford, C. C., Bridges, J. C., Schwenzer, S. P., Wiens, R. C., Rampe, E. B., Frydenvang, J., & Gasda, P. J. (2019). Alteration trends and geochemical source region characteristics preserved in the fluviolacustrine sedimentary record of Gale crater, Mars. *Geochimica et Cosmochimica Acta*, 246, 234–266. <https://doi.org/10.1016/j.gca.2018.11.031>
- Berger, J. A., Gellert, R., Boyd, N. I., King, P. L., McCraig, M. A., O’Connell-Cooper, C. D., Schmidt, M. E., Spray, J. G., et al. (2020). Elemental Composition and Chemical Evolution of Geologic Materials in Gale Crater, Mars: APXS Results From Bradbury Landing to the Vera Rubin Ridge. *Journal of Geophysical Research: Planets*, 125(12). <https://doi.org/10.1029/2020JE006536>
- Bibring, J.-P., Langevin, Y., Mustard, J. F., Poulet, F., Arvidson, R., Gendrin, A., Gondet, B., Mangold, N., et al. (2006). Global Mineralogical and Aqueous Mars History Derived from OMEGA/Mars Express Data. *Science*, 312(5772), 400–404. <https://doi.org/10.1126/science.1122659>

- Blake, D., Vaniman, D., Achilles, C., Anderson, R., Bish, D., Bristow, T., Chen, C., Chipera, S., et al. (2012). Characterization and Calibration of the CheMin Mineralogical Instrument on Mars Science Laboratory. *Space Science Reviews*, 170(1–4), 341–399. <https://doi.org/10.1007/s11214-012-9905-1>
- Blaney, D. L., Wiens, R. C., Maurice, S., Clegg, S. M., Anderson, R. B., Kah, L. C., Le Mouélic, S., Ollila, A., et al. (2014). Chemistry and texture of the rocks at Rocknest, Gale Crater: Evidence for sedimentary origin and diagenetic alteration: Rocknest Chemistry and Texture. *Journal of Geophysical Research: Planets*, 119(9), 2109–2131. <https://doi.org/10.1002/2013JE004590>
- Bridges, J. C., Schwenzer, S. P., Leveille, R., Westall, F., Wiens, R. C., Mangold, N., Bristow, T., Edwards, P., et al. (2015). Diagenesis and clay mineral formation at Gale Crater, Mars: Gale Crater Diagenesis. *Journal of Geophysical Research: Planets*, 120(1), 1–19. <https://doi.org/10.1002/2014JE004757>
- Bristow, T. F., Bish, D. L., Vaniman, D. T., Morris, R. V., Blake, D. F., Grotzinger, J. P., Rampe, E. B., Crisp, J. A., et al. (2015). The origin and implications of clay minerals from Yellowknife Bay, Gale crater, Mars. *American Mineralogist*, 100(4), 824–836. <https://doi.org/10.2138/am-2015-5077CCBYNCND>
- Bristow, T. F., Grotzinger, J. P., Rampe, E. B., Cuadros, J., Chipera, S. J., Downs, G. W., Fedo, C. M., Frydenvang, J., et al. (2021). Brine-driven destruction of clay minerals in Gale crater, Mars. *Science*, 373(6551), 198–204. <https://doi.org/10.1126/science.abg5449>
- Bristow, T. F., Rampe, E. B., Achilles, C. N., Blake, D. F., Chipera, S. J., Craig, P., Crisp, J. A., Des Marais, D. J., et al. (2018). Clay mineral diversity and abundance in sedimentary rocks of Gale crater, Mars. *Science Advances*, 4(6), eaar3330. <https://doi.org/10.1126/sciadv.aar3330>
- Burns, R.G. (1993) Rates and mechanisms of chemical weathering of ferromagnesian silicate minerals on Mars, *Geochimica et Cosmochimica Acta*, Volume 57, Issue 19, 1993, Pages 4555–4574, ISSN 0016-7037, [https://doi.org/10.1016/0016-7037\(93\)90182-V](https://doi.org/10.1016/0016-7037(93)90182-V).
- Carter, J., Poulet, F., Bibring, J.-P., Mangold, N., & Murchie, S. (2013). Hydrous minerals on Mars as seen by the CRISM and OMEGA imaging spectrometers: Updated global view: hydrous minerals on mars: Global view. *Journal of Geophysical Research: Planets*, 118(4), 831–858. <https://doi.org/10.1029/2012JE004145>
- Catling, D. C. (1999). A chemical model for evaporites on early Mars: Possible sedimentary tracers of the early climate and implications for exploration. *Journal of Geophysical Research: Planets*, 104(E7), 16453–16469. <https://doi.org/10.1029/1998JE001020>
- Chou, I-M., Seal, R. R., and Wang, A. (2013). The stability of sulfate and hydrated sulfate minerals near ambient conditions and their significance in environmental and planetary

941 sciences. *Journal of Asian Earth Sciences*, 62, 734–758. [https://](https://doi.org/10.1016/j.jseaes.2012.11.027)  
942 10.1016/j.jseaes.2012.11.027

943 Clark, B. C., Morris, R. V., McLennan, S. M., Gellert, R., Jolliff, B., Knoll, A. H., Squyres, S.  
944 W., Lowenstein, T. K., et al. (2005). Chemistry and mineralogy of outcrops at Meridiani  
945 Planum. *Earth and Planetary Science Letters*, 240(1), 73–94.  
946 <https://doi.org/10.1016/j.epsl.2005.09.040>

947 Cogram, P. (2018). Jarosite. Reference Module in Earth Systems and Environmental Sciences.  
948 Elsevier. doi: [10.1016/B978-0-12-409548-9.10960-1](https://doi.org/10.1016/B978-0-12-409548-9.10960-1)

949 David, G., Cousin, A., Forni, O., Meslin, P. -Y., Dehouck, E., Mangold, N., L’Haridon, J.,  
950 Rapin, W., et al. (2020). Analyses of High-Iron Sedimentary Bedrock and Diagenetic  
951 Features Observed With ChemCam at Vera Rubin Ridge, Gale Crater, Mars: Calibration  
952 and Characterization. *Journal of Geophysical Research: Planets*, 125(10).  
953 <https://doi.org/10.1029/2019JE006314>

954 Dehouck, E., McLennan, S. M., Meslin, P.-Y., & Cousin, A. (2014). Constraints on abundance,  
955 composition, and nature of X-ray amorphous components of soils and rocks at Gale  
956 crater, Mars: X-ray amorphous components at Gale. *Journal of Geophysical Research:*  
957 *Planets*, 119(12), 2640–2657. <https://doi.org/10.1002/2014JE004716>

958 Dehouck, E., McLennan, S. M., Sklute, E. C., & Dyar, M. D. (2017). Stability and fate of  
959 ferrihydrite during episodes of water/rock interactions on early Mars: An experimental  
960 approach: Stability of Ferrihydrite on Early Mars. *Journal of Geophysical Research:*  
961 *Planets*, 122(2), 358–382. <https://doi.org/10.1002/2016JE005222>

962 Elwood Madden et al., 2004

963 Fraeman, A. A., Edgar, L. A., Rampe, E. B., Thompson, L. M., Frydenvang, J., Fedo, C. M.,  
964 Catalano, J. G., Dietrich, W. E., et al. (2020). Evidence for a Diagenetic Origin of Vera  
965 Rubin Ridge, Gale Crater, Mars: Summary and Synthesis of *Curiosity* ’s Exploration  
966 Campaign. *Journal of Geophysical Research: Planets*, 125(12).  
967 <https://doi.org/10.1029/2020JE006527>

968 Fraeman, A. A., Ehlmann, B. L., Arvidson, R. E., Edwards, C. S., Grotzinger, J. P., Milliken, R.  
969 E., Quinn, D. P., & Rice, M. S. (2016). The stratigraphy and evolution of lower Mount  
970 Sharp from spectral, morphological, and thermophysical orbital data sets: Stratigraphy  
971 and Evolution of Mount Sharp. *Journal of Geophysical Research: Planets*, 121(9), 1713–  
972 1736. <https://doi.org/10.1002/2016JE005095>

973 Franz, H. B., McAdam, A. C., Ming, D. W., Freissinet, C., Mahaffy, P. R., Eldridge, D. L.,  
974 Fischer, W. W., Grotzinger, J. P., et al. (2017). Large sulfur isotope fractionations in  
975 Martian sediments at Gale crater. *Nature Geoscience*, 10(9), 658–662.  
976 <https://doi.org/10.1038/ngeo3002>

977 Frydenvang, J., Gasda, P. J., Hurowitz, J. A., Grotzinger, J. P., Wiens, R. C., Newsom, H. E.,  
978 Edgett, K. S., Watkins, J., et al. (2017). Diagenetic silica enrichment and late-stage

979 groundwater activity in Gale crater, Mars: Silica Enriching Diagenesis, Gale, Mars.  
 980 *Geophysical Research Letters*, 44(10), 4716–4724.  
 981 <https://doi.org/10.1002/2017GL073323>  
 982

983 Gabriel, T. S. J., Hardgrove, C., Achilles, C., Rampe, E. B., Czarnecki, S., Rapin, W., Nowicki,  
 984 S., Thompson, L. M., et al. (2019) Pervasive water-rich, fracture-associated alteration  
 985 halos in Gale crater, Mars. American Geophysical Union, Fall Meeting 2019, abstract  
 986 #P43B-08

987 Grant, J. A., Wilson, S. A., Mangold, N., Calef, F., & Grotzinger, J. P. (2014). The timing of  
 988 alluvial activity in Gale crater, Mars. *Geophysical Research Letters*, 41(4), 1142–1149.  
 989 <https://doi.org/10.1002/2013GL058909>

990 Grotzinger, J. P., Gupta, S., Malin, M. C., Rubin, D. M., Schieber, J., Siebach, K., Sumner, D.  
 991 Y., Stack, K. M., et al. (2015). Deposition, exhumation, and paleoclimate of an ancient  
 992 lake deposit, Gale crater, Mars. *Science*, 350(6257), aac7575–aac7575.  
 993 <https://doi.org/10.1126/science.aac7575>

994 Grotzinger, J. P., Sumner, D. Y., Kah, L. C., Stack, K., Gupta, S., Edgar, L., Rubin, D., Lewis,  
 995 K., et al. (2014). A Habitable Fluvio-Lacustrine Environment at Yellowknife Bay, Gale  
 996 Crater, Mars. *Science*, 343(6169), 1242777–1242777.  
 997 <https://doi.org/10.1126/science.1242777>

998 Hardie, L. W. A., & Eugster, H. P. (1970). The Evolution of Closed-Basin Brines. *Mineralogical*  
 999 *Society of America Special Paper*, 3, 273–290.

1000 Hausrath, E. M., Ming, D. W., Peretyazhko, T. S., & Rampe, E. B. (2018). Reactive transport  
 1001 and mass balance modeling of the Stimson sedimentary formation and altered fracture  
 1002 zones constrain diagenetic conditions at Gale crater, Mars. *Earth and Planetary Science*  
 1003 *Letters*, 491, 1–10. <https://doi.org/10.1016/j.epsl.2018.02.037>

1004 Horgan, B. H. N., Johnson, J. R., Fraeman, A. A., Rice, M. S., Seeger, C., Bell, J. F., Bennett, K.  
 1005 A., Cloutis, et al. (2020). Diagenesis of Vera Rubin Ridge, Gale Crater, Mars, From  
 1006 Mastcam Multispectral Images. *Journal of Geophysical Research: Planets*, 125(11).  
 1007 <https://doi.org/10.1029/2019JE006322>

1008 Hurowitz, J. A., Grotzinger, J. P., Fischer, W. W., McLennan, S. M., Milliken, R. E., Stein, N.,  
 1009 Vasavada, A. R., Blake, D. F., et al. (2017). Redox stratification of an ancient lake in  
 1010 Gale crater, Mars. *Science*, 356(6341), eaah6849.  
 1011 <https://doi.org/10.1126/science.aah6849>

1012 Ishiguro, M., Makino, T., & Hattori, Y. (2006). Sulfate adsorption and surface precipitation on a  
 1013 volcanic ash soil (allophanic andisol). *Journal of Colloid and Interface Science*, 300(2),  
 1014 504–510. <https://doi.org/10.1016/j.jcis.2006.04.032>

1015 Jara, A.A., Violante, A., Pigna, M., and de la Luz Mora, M. (2006). Mutual interactions of  
 1016 sulfate, oxalate, citrate, and phosphate on synthetic and natural allophanes. *Soil Science*  
 1017 *Society of America Journal*, 70, 337–346.

- 1018 Jia, C., Wu, L., Chen, Q., Ke, P., De Yoreo, J. J., & Guan, B. (2020). Structural evolution of  
1019 amorphous calcium sulfate nanoparticles into crystalline gypsum phase. *CrystEngComm*,  
1020 22(41), 6805–6810. <https://doi.org/10.1039/D0CE01173H>
- 1021 Jia, C., Wu, L., Fulton, J. L., Liang, X., De Yoreo, J. J., & Guan, B. (2021). Structural  
1022 Characteristics of Amorphous Calcium Sulfate: Evidence to the Role of Water  
1023 Molecules. *The Journal of Physical Chemistry C*, 125(6), 3415–3420.  
1024 <https://doi.org/10.1021/acs.jpcc.0c10016>
- 1025 Kah, L. C., Stack, K. M., Eigenbrode, J. L., Yingst, R. A., & Edgett, K. S. (2018).  
1026 Syndepositional precipitation of calcium sulfate in Gale Crater, Mars. *Terra Nova*, 30(6),  
1027 431–439. <https://doi.org/10.1111/ter.12359>
- 1028 King, P. L., & McLennan, S. M. (2010). Sulfur on Mars. *Elements*, 6 (2), 107–112. doi:  
1029 <https://doi.org/10.2113/gselements.6.2.107>
- 1030 Klug, H. P., & Alexander, L. E. (1974). X-ray diffraction procedures: For polycrystalline and  
1031 amorphous materials (2nd ed.). John Wiley and Sons.
- 1032 Kronyak, R. E., Kah, L. C., Miklusick, N. B., Edgett, K. S., Sun, V. Z., Bryk, A. B., &  
1033 Williams, R. M. E. (2019). Extensive Polygonal Fracture Network in Siccar Point group  
1034 Strata: Fracture Mechanisms and Implications for Fluid Circulation in Gale Crater, Mars.  
1035 *Journal of Geophysical Research: Planets*, 124(10), 2613–2634.  
1036 <https://doi.org/10.1029/2019JE006125>
- 1037 Le Deit, L., Hauber, E., Fueten, F., Pondrelli, M., Rossi, A. P., & Jaumann, R. (2013). Sequence  
1038 of infilling events in Gale Crater, Mars: Results from morphology, stratigraphy, and  
1039 mineralogy: Sedimentary infilling in gale crater. *Journal of Geophysical Research:*  
1040 *Planets*, 118(12), 2439–2473. <https://doi.org/10.1002/2012JE004322>
- 1041 **Léveillé et al., 2014**
- 1042 L’Haridon, J., Mangold, N., Fraeman, A. A., Johnson, J. R., Cousin, A., Rapin, W., David, G.,  
1043 Dehouck, E., et al. (2020). Iron Mobility During Diagenesis at Vera Rubin Ridge, Gale  
1044 Crater, Mars. *Journal of Geophysical Research: Planets*, 125(11).  
1045 <https://doi.org/10.1029/2019JE006299>
- 1046 Mahaffy, P. R., Webster, C. R., Cabane, M., Conrad, P. G., Coll, P., Atreya, S. K., Arvey, R.,  
1047 Barciniak, M., et al. (2012). The Sample Analysis at Mars Investigation and Instrument  
1048 Suite. *Space Science Reviews*, 170(1–4), 401–478. [https://doi.org/10.1007/s11214-012-](https://doi.org/10.1007/s11214-012-9879-z)  
1049 [9879-z](https://doi.org/10.1007/s11214-012-9879-z)
- 1050 Malin, M. C., & Edgett, K. S. (2000). Sedimentary Rocks of Early Mars. *Science*, 290(5498),  
1051 1927–1937. <https://doi.org/10.1126/science.290.5498.1927>
- 1052 Mangold, N., Dehouck, E., Fedo, C., Forni, O., Achilles, C., Bristow, T., Downs, R. T.,  
1053 Frydenvang, J., et al. (2019). Chemical alteration of fine-grained sedimentary rocks at  
1054 Gale crater. *Icarus*, 321, 619–631. <https://doi.org/10.1016/j.icarus.2018.11.004>

- 1055 Martin, P. E., Farley, K. A., Baker, M. B., Malespin, C. A., Schwenzer, S. P., Cohen, B. A.,  
1056 Mahaffy, P. R., McAdam, A. C., et al. (2017). A Two-Step K-Ar Experiment on Mars:  
1057 Dating the Diagenetic Formation of Jarosite from Amazonian Groundwaters: A two-step  
1058 K-Ar experiment on Mars. *Journal of Geophysical Research: Planets*, 122(12), 2803–  
1059 2818. <https://doi.org/10.1002/2017JE005445>
- 1060 McAdam, A. C., Franz, H. B., Sutter, B., Archer, P. D., Freissinet, C., Eigenbrode, J. L., Ming,  
1061 D. W., Atreya, S. K., et al. (2014). Sulfur-bearing phases detected by evolved gas  
1062 analysis of the Rocknest aeolian deposit, Gale Crater, Mars: Rocknest sulfur phases  
1063 detected by SAM. *Journal of Geophysical Research: Planets*, 119(2), 373–393.  
1064 <https://doi.org/10.1002/2013JE004518>
- 1065 McAdam, A. C., Knudson, C. A., Sutter, B., Franz, H. B., Archer Jr, P. D., Eigenbrode, J. L.,  
1066 Ming, D. W., Morris, R. V., et al. (2016). Reactions involving calcium and magnesium  
1067 sulfates as potential sources of sulfur dioxide during MSL SAM evolved gas analyses.  
1068 *Abstract #2277*.
- 1069 McAdam, A. C., Sutter, B., Archer, P. D., Franz, H. B., Wong, G. M., Lewis, J. M. T.,  
1070 Eigenbrode, J. L., Stern, J. C., et al. (2020). Constraints on the Mineralogy and  
1071 Geochemistry of Vera Rubin Ridge, Gale Crater, Mars, From Mars Science Laboratory  
1072 Sample Analysis at Mars Evolved Gas Analyses. *Journal of Geophysical Research:*  
1073 *Planets*, 125(11). <https://doi.org/10.1029/2019JE006309>
- 1074 McLennan, S. M. (2014)
- 1075 McLennan, S. M. and Grotzinger, J. P. (2008) The sedimentary rock cycle of Mars. In: J. F. Bell  
1076 III (ed.) *The Martian Surface: Composition, Mineralogy, and Physical Properties*.  
1077 Cambridge Univ. Press (Cambridge), pp. 541-577.
- 1078 Meyer, C. (2008) *The Martian Meteorite Compendium*,  
1079 <http://curator.jsc.nasa.gov/antmet/mmc/index.cfm>  
1080
- 1081 Milliken, R. E., Grotzinger, J. P., & Thomson, B. J. (2010). Paleoclimate of Mars as captured by  
1082 the stratigraphic record in Gale Crater: Stratigraphy of Gale crater. *Geophysical Research*  
1083 *Letters*, 37(4). <https://doi.org/10.1029/2009GL041870>
- 1084 Morris, R. V., Klingelhöfer, G., Schröder, C., Rodionov, D. S., Yen, A., Ming, D. W., de Souza,  
1085 P. A., Wdowiak, T., et al. (2006). Mössbauer mineralogy of rock, soil, and dust at  
1086 Meridiani Planum, Mars: Opportunity's journey across sulfate-rich outcrop, basaltic sand  
1087 and dust, and hematite lag deposits: Iron mineralogy at meridiani planum. *Journal of*  
1088 *Geophysical Research: Planets*, 111(E12), n/a-n/a.  
1089 <https://doi.org/10.1029/2006JE002791>
- 1090 Morris, R.V., Rampe, E.B., Graff, T. G., Archer, P. D., Jr., Le, L., Ming, D. W., & Sutter, B.  
1091 (2015). Transmission X-ray diffraction (XRD) patterns relevant to the MSL CheMin  
1092 amorphous component: Sulfates and silicates. 46th LPSC, Abstract #2434, Houston, TX.



- 1093 Morris, R. V., Vaniman, D. T., Blake, D. F., Gellert, R., Chipera, S. J., Rampe, E. B., Ming, D.  
1094 W., Morrison, S. M., et al. (2016). Silicic volcanism on Mars evidenced by tridymite in  
1095 high-SiO<sub>2</sub> sedimentary rock at Gale crater. *Proceedings of the National Academy of*  
1096 *Sciences*, 113(26), 7071–7076. <https://doi.org/10.1073/pnas.1607098113>
- 1097 Morris, R.V., Vaniman, D.T., Clark, J.V., Rampe, E.B., Ming, D.W., Achilles, C.N., and Archer,  
1098 D.P. (2021). Toward understanding ferruginous smectite Mg for Ca interlayer cation  
1099 exchange, crystalline Ca-sulfates, and amorphous Mg-sulfates on Mars. 52nd LPSC,  
1100 Abstract #2548, Virtual.
- 1101 Morrison, S. M., Downs, R. T., Blake, D. F., Vaniman, D. T., Ming, D. W., Hazen, R. M.,  
1102 Treiman, A. H., Achilles, C. N., et al. (2018). Crystal chemistry of martian minerals from  
1103 Bradbury Landing through Naukluft Plateau, Gale crater, Mars. *American Mineralogist*,  
1104 103(6), 857–871. <https://doi.org/10.2138/am-2018-6124>
- 1105 Mu, J., & Perlmutter, D. D. (1981). Thermal decomposition of inorganic sulfates and their  
1106 hydrates. *Industrial & Engineering Chemistry Process Design and Development*, 20(4),  
1107 640–646. <https://doi.org/10.1021/i200015a010>
- 1108 Murchie, S. L., Mustard, J. F., Ehlmann, B. L., Milliken, R. E., Bishop, J. L., McKeown, N. K.,  
1109 Noe Dobrea, E. Z., Seelos, F. P., et al. (2009). A synthesis of Martian aqueous  
1110 mineralogy after 1 Mars year of observations from the Mars Reconnaissance Orbiter.  
1111 *Journal of Geophysical Research*, 114, E00D06. <https://doi.org/10.1029/2009JE003342>
- 1112 Nachon, M., Clegg, S. M., Mangold, N., Schröder, S., Kah, L. C., Dromart, G., Ollila, A.,  
1113 Johnson, J. R., et al. (2014). Calcium sulfate veins characterized by ChemCam/Curiosity  
1114 at Gale crater, Mars: Calcium sulfate veins at gale crater. *Journal of Geophysical*  
1115 *Research: Planets*, 119(9), 1991–2016. <https://doi.org/10.1002/2013JE004588>
- 1116 Nachon, M., Mangold, N., Forni, O., Kah, L. C., Cousin, A., Wiens, R. C., Anderson, R., Blaney,  
1117 D., et al. (2017). Chemistry of diagenetic features analyzed by ChemCam at Pahrump  
1118 Hills, Gale crater, Mars. *Icarus*, 281, 121–136.  
1119 <https://doi.org/10.1016/j.icarus.2016.08.026>  
1120
- 1121 Newsom, H., Belgacem, I., Jackson, R., Ha, B., Vaci, Z., et al. (2016). The materials at an  
1122 unconformity between the Murray and Stimson formations at Marias Pass, Gale Crater,  
1123 Mars. Lunar and Planetary Science Conference, Mar 2016, Houston, TX, United States.
- 1124 Rampe, E. B., Blake, D. F., Bristow, T. F., Ming, D. W., Vaniman, D. T., Morris, R. V.,  
1125 Achilles, C. N., Chipera, S. J., et al. (2020). Mineralogy and geochemistry of sedimentary  
1126 rocks and eolian sediments in Gale crater, Mars: A review after six Earth years of  
1127 exploration with Curiosity. *Geochemistry*, 80(2), 125605.  
1128 <https://doi.org/10.1016/j.chemer.2020.125605>
- 1129 Rampe, E. B., Bristow, T. F., Morris, R. V., Morrison, S. M., Achilles, C. N., Ming, D. W.,  
1130 Vaniman, D. T., Blake, D. F., et al. (2020). Mineralogy of Vera Rubin Ridge from the  
1131 Mars Science Laboratory CheMin Instrument. *Journal of Geophysical Research: Planets*,  
1132 125(9). <https://doi.org/10.1029/2019JE006306>



- 1133 Rampe, E. B., Ming, D. W., Blake, D. F., Bristow, T. F., Chipera, S. J., Grotzinger, J. P., Morris,  
1134 R. V., Morrison, S. M., et al. (2017). Mineralogy of an ancient lacustrine mudstone  
1135 succession from the Murray formation, Gale crater, Mars. *Earth and Planetary Science*  
1136 *Letters*, 471, 172–185. <https://doi.org/10.1016/j.epsl.2017.04.021>
- 1137 Rampe, E. B., Morris, R. V., Archer, P. D., Agresti, D. G., & Ming, D. W. (2016). Recognizing  
1138 sulfate and phosphate complexes chemisorbed onto nanophase weathering products on  
1139 Mars using in-situ and remote observations. *American Mineralogist*, 101(3), 678–689.  
1140 <https://doi.org/10.2138/am-2016-5408CCBYNCND>
- 1141 Rapin, W., Ehlmann, B. L., Dromart, G., Schieber, J., Thomas, N. H., Fischer, W. W., Fox, V.  
1142 K., Stein, N. T., et al. (2019). An interval of high salinity in ancient Gale crater lake on  
1143 Mars. *Nature Geoscience*, 12(11), 889–895. <https://doi.org/10.1038/s41561-019-0458-8>
- 1144 Rapin, W., Meslin, P.-Y., Maurice, S., Vaniman, D., Nachon, M., Mangold, N., Schröder, S.,  
1145 Gasnault, O., et al. (2016). Hydration state of calcium sulfates in Gale crater, Mars:  
1146 Identification of bassanite veins. *Earth and Planetary Science Letters*, 452, 197–205.  
1147 <https://doi.org/10.1016/j.epsl.2016.07.045>
- 1148 Rice, M. S., Gupta, S., Treiman, A. H., Stack, K. M., Calef, F., Edgar, L. A., Grotzinger, J.,  
1149 Lanza, N., et al. (2017). Geologic overview of the Mars Science Laboratory rover  
1150 mission at the Kimberley, Gale crater, Mars: Overview of MSL at the Kimberley. *Journal*  
1151 *of Geophysical Research: Planets*, 122(1), 2–20. <https://doi.org/10.1002/2016JE005200>
- 1152 Rivera-Hernández, F., Sumner, D. Y., Mangold, N., Banham, S. G., Edgett, K. S., Fedo, C. M.,  
1153 Gupta, S., Gwizd, S., et al. (2020). Grain Size Variations in the Murray Formation:  
1154 Stratigraphic Evidence for Changing Depositional Environments in Gale Crater, Mars.  
1155 *Journal of Geophysical Research: Planets*, 125(2).  
1156 <https://doi.org/10.1029/2019JE006230>
- 1157 Sheppard, R. Y., Milliken, R. E., Parente, M., & Itoh, Y. (2021a). Updated Perspectives and  
1158 Hypotheses on the Mineralogy of Lower Mt. Sharp, Mars, as Seen from Orbit. *Journal of*  
1159 *Geophysical Research: Planets*, 126(2). <https://doi.org/10.1029/2020JE006372>
- 1160 Sheppard, R. Y., Milliken, R. E., & Robertson, K. M. (2021b). *Presence of clay minerals can*  
1161 *obscure spectral evidence of Mg-sulfates: Implications for orbital observations of Mars.*  
1162 Presented at the 52nd Lunar and Planetary Science Conference, Abstract #1560.
- 1163 Siebach, K. L., Grotzinger, J. P., Kah, L. C., Stack, K. M., Malin, M., Léveillé, R., & Sumner, D.  
1164 Y. (2014). Subaqueous shrinkage cracks in the Sheepbed mudstone: Implications for  
1165 early fluid diagenesis, Gale crater, Mars. *Journal of Geophysical Research: Planets*,  
1166 119(7), 1597–1613. <https://doi.org/10.1002/2014JE004623>
- 1167 Sklute, E. C., Jensen, H. B., Rogers, A. D., & Reeder, R. J. (2015). Morphological, structural,  
1168 and spectral characteristics of amorphous iron sulfates. *Journal of Geophysical Research:*  
1169 *Planets*, 120(4), 809–830. <https://doi.org/10.1002/2014JE004784>

- 1170 Sklute, E. C., Rogers, A. D., Gregerson, J. C., Jensen, H. B., Reeder, R. J., & Dyar, M. D.  
1171 (2018). Amorphous salts formed from rapid dehydration of multicomponent chloride and  
1172 ferric sulfate brines: Implications for Mars. *Icarus*, 302, 285–295.  
1173 <https://doi.org/10.1016/j.icarus.2017.11.018>
- 1174 Smith, R. (2021), “X-ray amorphous sulfur-bearing phases in sedimentary rocks of Gale crater,  
1175 Mars - Supplemental”, *Mendeley Data*, V1, doi: 10.17632/8b5yj38wx3.1
- 1176 Smith, R. J., & Horgan, B. H. N. (2021). Nanoscale Variations in Natural Amorphous and  
1177 Nanocrystalline Weathering Products in Mafic to Intermediate Volcanic Terrains on  
1178 Earth: Implications for Amorphous Detections on Mars. *Journal of Geophysical*  
1179 *Research: Planets*, 126(5). <https://doi.org/10.1029/2020JE006769>
- 1180 Smith, R. J., McLennan, S. M., Achilles, C. N., Dehouck, E., Horgan, B. H. N., Mangold, N.,  
1181 Rampe, E. B., Salvatore, M., et al. (2021). X-Ray Amorphous Components in  
1182 Sedimentary Rocks of Gale Crater, Mars: Evidence for Ancient Formation and Long-  
1183 Lived Aqueous Activity. *Journal of Geophysical Research: Planets*, 126(3).  
1184 <https://doi.org/10.1029/2020JE006782>
- 1185 **Smith, R. J. et al. (2018)**
- 1186 Stack, K. M., Grotzinger, J. P., Kah, L. C., Schmidt, M. E., Mangold, N., Edgett, K. S., Sumner,  
1187 D. Y., Siebach, K. L., et al. (2014). Diagenetic origin of nodules in the Sheepbed  
1188 member, Yellowknife Bay formation, Gale crater, Mars: Diagenetic Nodules in Gale  
1189 Crater. *Journal of Geophysical Research: Planets*, 119(7), 1637–1664.  
1190 <https://doi.org/10.1002/2014JE004617>
- 1191 Stein, N., Grotzinger, J. P., Schieber, J., Mangold, N., Hallet, B., Newsom, H., Stack, K. M.,  
1192 Berger, J. A., et al. (2018). Desiccation cracks provide evidence of lake drying on Mars,  
1193 Sutton Island member, Murray formation, Gale Crater. *Geology*, 46(6), 515–518.  
1194 <https://doi.org/10.1130/G40005.1>
- 1195 Sun, V. Z., Stack, K. M., Kah, L. C., Thompson, L., Fischer, W., Williams, A. J., Johnson, S. S.,  
1196 Wiens, R. C., et al. (2019). Late-stage diagenetic concretions in the Murray formation,  
1197 Gale crater, Mars. *Icarus*, 321, 866–890. <https://doi.org/10.1016/j.icarus.2018.12.030>
- 1198 Sutter, B., McAdam, A. C., Mahaffy, P. R., Ming, D. W., Edgett, K. S., Rampe, E. B.,  
1199 Eigenbrode, J. L., Franz, H. B., et al. (2017). Evolved gas analyses of sedimentary rocks  
1200 and eolian sediment in Gale Crater, Mars: Results of the Curiosity rover’s sample  
1201 analysis at Mars instrument from Yellowknife Bay to the Namib Dune. *Journal of*  
1202 *Geophysical Research*, 122, 2574–2609. <https://doi.org/10.1002/2016JE005225>
- 1203 Swift, W. M., Panek, A. F., Smith, G. W., Vogel, G. J., & Jonke, A. A. (1976). *Decomposition of*  
1204 *calcium sulfate: A review of the literature*. (ANL--76-122, 7224692; p. ANL--76-122,  
1205 7224692). <https://doi.org/10.2172/7224692>
- 1206 Thompson, L. M., Berger, J. A., Spray, J. G., Fraeman, A. A., McCraig, M. A., O’Connell-  
1207 Cooper, C. D., Schmidt, M. E., VanBommel, et al. (2020). APXS-Derived Compositional

- 1208 Characteristics of Vera Rubin Ridge and Murray Formation, Gale Crater, Mars:  
1209 Geochemical Implications for the Origin of the Ridge. *Journal of Geophysical Research:*  
1210 *Planets*, 125(10). <https://doi.org/10.1029/2019JE006319>
- 1211 Thomson, B. J., Bridges, N. T., Milliken, R., Baldrige, A., Hook, S. J., Crowley, J. K., Marion,  
1212 G. M., de Souza Filho, et al. (2011). Constraints on the origin and evolution of the  
1213 layered mound in Gale Crater, Mars using Mars Reconnaissance Orbiter data. *Icarus*,  
1214 214(2), 413–432. <https://doi.org/10.1016/j.icarus.2011.05.002>
- 1215 Thorpe, M. T., Hurowitz, J. A., & Siebach, K. L. (2021). Source-to-Sink Terrestrial Analogs for  
1216 the Paleoenvironment of Gale Crater, Mars. *Journal of Geophysical Research: Planets*,  
1217 126(2). <https://doi.org/10.1029/2020JE006530>
- 1218 Tosca, N. J., Ahmed, I. A. M., Tutolo, B. M., Ashpitel, A., & Hurowitz, J. A. (2018). Magnetite  
1219 authigenesis and the warming of early Mars. *Nature Geoscience*, 11(9), 635–639.  
1220 <https://doi.org/10.1038/s41561-018-0203-8>
- 1221 Tosca, N. J., & McLennan, S. M. (2009). Experimental constraints on the evaporation of  
1222 partially oxidized acid-sulfate waters at the martian surface. *Geochimica et*  
1223 *Cosmochimica Acta*, 73(4), 1205–1222. <https://doi.org/10.1016/j.gca.2008.11.015>
- 1224 Tosca, N. J., McLennan, S. M., Clark, B. C., Grotzinger, J. P., Hurowitz, J. A., Knoll, A. H.,  
1225 Schröder, C., & Squyres, S. W. (2005). Geochemical modeling of evaporation processes  
1226 on Mars: Insight from the sedimentary record at Meridiani Planum. *Earth and Planetary*  
1227 *Science Letters*, 240(1), 122–148. <https://doi.org/10.1016/j.epsl.2005.09.042>
- 1228 Treiman, A. H., Bish, D. L., Vaniman, D. T., Chipera, S. J., Blake, D. F., Ming, D. W., Morris,  
1229 R. V., Bristow, T. F., et al. (2016). Mineralogy, provenance, and diagenesis of a potassic  
1230 basaltic sandstone on Mars: CheMin X-ray diffraction of the Windjana sample  
1231 (Kimberley area, Gale Crater). *Journal of Geophysical Research: Planets*, 121(1), 75–  
1232 106. <https://doi.org/10.1002/2015JE004932>
- 1233 Usui, T., Alexander, C. M. O., Wang, J., Simon, J. I., & Jones, J. H. (2012). Origin of water and  
1234 mantle–crust interactions on Mars inferred from hydrogen isotopes and volatile element  
1235 abundances of olivine-hosted melt inclusions of primitive shergottites. *Earth and*  
1236 *Planetary Science Letters*, 357–358, 119–129. <https://doi.org/10.1016/j.epsl.2012.09.008>
- 1237 **VanBommel, S. J., (2016)**
- 1238 VanBommel, S. J., Gellert, R., Berger, J. A., Thompson, L. M., Edgett, K. S., McBride, M. J.,  
1239 Minitti, M. E., Boyd, N. I., et al. (2017). Modeling and mitigation of sample relief effects  
1240 applied to chemistry measurements by the Mars Science Laboratory Alpha Particle X-ray  
1241 Spectrometer: Target relief effect mitigation and modeling for the MSL APXS. *X-Ray*  
1242 *Spectrometry*, 46(4), 229–236. <https://doi.org/10.1002/xrs.2755>
- 1243 Vaniman, D. T. & Chipera, S. J. (2006). Transformations of Mg- and Ca-sulfate hydrates in Mars  
1244 regolith. *American Mineralogist*, 91(10), 1628–1642. [https://doi-](https://doi-org.proxy.library.stonybrook.edu/10.2138/am.2006.2092)  
1245 [org.proxy.library.stonybrook.edu/10.2138/am.2006.2092](https://doi-org.proxy.library.stonybrook.edu/10.2138/am.2006.2092)

- 1246 Vaniman, D. T., Bish, D. L., Chipera, S. J., Fialips, C. I., William Carey, J., & Feldman, W. C.  
1247 (2004). Magnesium sulphate salts and the history of water on Mars. *Nature*, 431(7009),  
1248 663–665. <https://doi.org/10.1038/nature02973>
- 1249 Vaniman, D. T., Bish, D. L., Ming, D. W., Bristow, T. F., Morris, R. V., Blake, D. F., Chipera,  
1250 S. J., Morrison, S. M., et al. (2014). Mineralogy of a Mudstone at Yellowknife Bay, Gale  
1251 Crater, Mars. *Science*, 343(6169), 1243480–1243480.  
1252 <https://doi.org/10.1126/science.1243480>
- 1253 Vaniman, D. T., Martínez, G. M., Rampe, E. B., Bristow, T. F., Blake, D. F., Yen, A. S., Ming,  
1254 D. W., Rapin, W., et al. (2018). Gypsum, bassanite, and anhydrite at Gale crater, Mars.  
1255 *American Mineralogist*, 103(7), 1011–1020. <https://doi.org/10.2138/am-2018-6346>
- 1256 Wang, A., & Zhou, Y. (2014). Experimental comparison of the pathways and rates of the  
1257 dehydration of Al-, Fe-, Mg- and Ca-sulfates under Mars relevant conditions. *Icarus*, 234,  
1258 162–173. <https://doi.org/10.1016/j.icarus.2014.02.003>
- 1259 Wang, A., Freeman, J. J., & Jolliff, B. L. (2009). Phase transition pathways of the hydrates of  
1260 magnesium sulfate in the temperature range 50°C to 5°C: Implication for sulfates on  
1261 Mars. *Journal of Geophysical Research*, 114(E4), E04010.  
1262 <https://doi.org/10.1029/2008JE003266>
- 1263 Wang, Y.-W., Kim, Y.-Y., Christenson, H. K., & Meldrum, F. C. (2012). A new precipitation  
1264 pathway for calcium sulfate dihydrate (gypsum) via amorphous and hemihydrate  
1265 intermediates. *Chem. Commun.*, 48(4), 504–506. <https://doi.org/10.1039/C1CC14210K>
- 1266 Watkins, J. A., Grotzinger, J., Stein, N., Banham, S. G., Gupta, S., Rubin, D., Stack, K. M., &  
1267 Edgett, K. S. (2016). *Paleotopography of erosional unconformity, base of Stimson*  
1268 *formation, Gale crater, Mars. Abstract #2939, 2.*
- 1269 Wiens, R. C., Maurice, S., Barraclough, B., Saccoccio, M., Barkley, W. C., Bell, J. F., Bender,  
1270 S., Bernardin, J., et al. (2012). The ChemCam Instrument Suite on the Mars Science  
1271 Laboratory (MSL) Rover: Body Unit and Combined System Tests. *Space Science*  
1272 *Reviews*, 170(1–4), 167–227. <https://doi.org/10.1007/s11214-012-9902-4>
- 1273 Worden, R. H., & Burley, S. D. (2003). Sandstone Diagenesis: The Evolution of Sand to Stone.  
1274 In S. D. Burley & R. H. Worden (Eds.), *Sandstone Diagenesis* (pp. 1–44). Blackwell  
1275 Publishing Ltd. <https://doi.org/10.1002/9781444304459.ch>
- 1276 Yen, A. S., Ming, D. W., Vaniman, D. T., Gellert, R., Blake, D. F., Morris, R. V., Morrison, S.  
1277 M., Bristow, T. F., et al. (2017). Multiple stages of aqueous alteration along fractures in  
1278 mudstone and sandstone strata in Gale Crater, Mars. *Earth and Planetary Science Letters*,  
1279 471, 186–198. <https://doi.org/10.1016/j.epsl.2017.04.033>  
1280